IRAQI JOURNAL OF APPLIED PHYSICS

The *Iraqi Journal of Applied Physics (IJAP)* is a peer reviewed journal of high quality devoted to the publication of original research papers from applied physics and their broad range of applications. IJAP publishes quality original research papers, comprehensive review articles, survey articles, book reviews, dissertation abstracts in physics and its applications in the broadest sense. It is intended that the journal may act as an interdisciplinary forum for Physics and its applications. Innovative applications and material that brings together diverse areas of Physics are particularly welcome. Review articles in selected areas are published from time to time. It aims to disseminate knowledge; provide a learned reference in the field; and establish channels of communication between academic and research experts, policy makers and executives in industry, commerce and investment institutions. IJAP is a quarterly specialized periodical dedicated to publishing original papers, letters and reviews in: Applied & Nonlinear Optics, Applied Mechanics & Thermodynamics, Digital & Optical Communications, Electronic Materials & Devices, Laser Physics & Applications, Plasma Physics & Applications, Quantum Physics & Spectroscopy, Semiconductors & Optoelectronics, and Solid State Physics & Applications

SPONSORED AND PUBLISHED BY
THE IRAQI SOCIETY FOR ALTERNATIVE AND RENEWABLE ENERGY SOURCES & TECHNIQUES (I.S.A.R.E.S.T.)

ISSN 1813-2065

IRAQI JOURNAL OF APPLIED PHYSICS
" INSTRUCTIONS TO AUTHORS "

CONTRIBUTIONS
Contributions to be published in this journal should be original research works, i.e., those not already published or submitted for publication elsewhere, individual papers or letters to editor.

SUBMISSION OF MANUSCRIPTS
Manuscripts should be submitted to the editor at the mailing address:
Iraqi Journal of Applied Physics
Editorial Board
P. O. Box 55259, Baghdad 12001, IRAQ, submission@ijap.org , editor@ijap.org

MANUSCRIPTS
Two hard copies with soft copy on a compact disc (CD) should be submitted to Editor in the following configuration:
- Double-spaced one-side A4 size with 2.5 cm margins of all sides
- Times New Roman font (16pt bold for title, 14pt bold for names, 12pt bold for headings, 12pt regular for text)
- Letters should not exceed 10 pages, papers should not exceed 20 pages and reviews are up to author.
- Manuscripts presented in English only are accepted.
- English abstract not exceed 150 words
- 4 keywords (at least) should be maintained on (PACS preferred)
- Author(s) should express all quantities in SI units
- Equations should be written in equation form (*italic* and symbolic)
- Figures and Tables should be separated from text
- Figures and diagrams can be submitted in colors for assessment and they will be returned to authors after provide printable copies
- Charts should be indicated by the software used for
- Only original or high-resolution scanner photos are accepted
- For electronic submission, articles should be formatted with MS-Word software.

AUTHOR NAMES AND AFFILIATIONS
It is IJAP policy that all those who have participated significantly in the technical aspects of a paper be recognized as co-authors or cited in the acknowledgments. In the case of a paper with more than one author, correspondence concerning the paper will be sent to the first author unless staff is advised otherwise.
Author name should consist of first name, middle initial, last name. The author affiliation should consist of the following, as applicable, in the order noted:
- Company or college (with department name or company division)
- Postal address
- City, state, zip code
- Country name
- Telephone, and e-mail

REFERENCES
The references should be brought at the end of the article, and numbered in the order of their appearance in the paper. The reference list should be cited in accordance with the following examples:
[1] X. Ning and M.R. Lovell, "On the Sliding Friction Characteristics of Unidirectional Continuous FRP Composites", *ASME J. Tribol.*, 124(1) (2002) 5-13.
[2] M. Barnes, "Stresses in Solenoids", *J. Appl. Phys.*, 48(5) (2001) 2000–2008.
[3] J. Jones, "Contact Mechanics", Cambridge University Press (Cambridge, UK) (2000), Ch.6, p.56.
[4] Y. Lee, S.A. Korpela and R. Horne, "Structure of Multi-Cellular Natural Convection in a Tall Vertical Annulus", Proc. 7th International Heat Transfer Conference, U. Grigul et al., eds., Hemisphere (Washington DC), 2 (1982) 221–226.
[5] M. Hashish, "Waterjet Technology Development", High Pressure Technology, PVP-Vol. 406 (2000), 135-140.
[6] D.W. Watson, "Thermodynamic Analysis", ASME Paper No. 97-GT-288 (1997).
[7] C.Y. Tung, "Evaporative Heat Transfer in the Contact Line of a Mixture", Ph.D. thesis, Rensselaer Polytechnic Institute, Troy, NY (1982).

PROOFS
Authors will receive proofs of papers and are requested to return one corrected hard copy with a WORD copy on a compact disc (CD). New materials inserted in the original text without Editor permission may cause rejection of paper.

COPYRIGHT FORM
Author(s) will be asked to transfer copyrights of the article to the Journal soon after acceptance of it. This will ensure the widest possible dissemination of information.

OFFPRINTS
Authors will receive offprints free of charge and any additional offprints can be ordered.

SUBSCRIPTION AND ORDERS
Annual fees (4 issues per year) of subscription are:
- 50 US$ for individuals inside Iraq.
- 100 US$ for establishments inside Iraq.
- 100 US$ for individuals abroad.
- 200 US$ for establishments abroad.

Fees are reduced by 25% for I.S.A.R.E.S.T. members. Orders of issues can be submitted by contacting the editor-in-chief or editorial office at **subscription@ijap.org** to maintain the address of issue delivery and payment way.

Phase Noise Compensation for Coherent Orthogonal Frequency Division Multiplexing in Optical Fiber Communications Systems

Jassim K. Hmood

Department of Laser and Optoelectronics Engineering, University of Technology, Baghdad, Iraq
jassim_711@yahoo.com

In this paper, the Coherent Optical (CO) systems using Orthogonal Frequency Division Multiplexing (OFDM) for dispersion compensation is demonstrated. The Quadrature Amplitude Modulation QAM-OFDM transmitter signal was controlled by the Mach-Zender Modulator (MZM) which modulates the laser source with wavelength of 1550nm. The heterodyne receiver with dual-polarization optoelectronic down-converter is used to obtain good coherent detection without using optical phase locked loop. The analytical part was done using a software simulator. All the proposed system components were simulated using VPIphotonic simulation software for testing CO-OFDM system. The transmitted signal, optical spectrum, eye diagram and constellation diagram was obtained to evaluate system performance.

Keywords: Optical fibers, OFDM, Coherent communications, Heterodyne
Received: 26 March 2009, **Revised**: 3 May 2009, **Accepted**: 10 May 2009

1. Introduction

Orthogonal frequency-division multiplexing (OFDM) is a multi-carrier technique that has been deployed in optical fiber communications. A multi-carrier system sends information over N-frequency-division-multiplexed (FDM) channels, each modulated by a different carrier. The total bit rate of the OFDM stream is the sum of bit rates in all narrowband channels. These narrowband channels are also called tones and OFDM is also called multi-tone modulation. Each tone in OFDM can use a different modulation inside it, for example, BPSK, QPSK, and QAM [1]. Coherent optical OFDM (CO-OFDM) has been proposed to combat fiber chromatic and polarization-mode dispersion [2]. Therefore, it can be used to compensate for fiber chromatic dispersion in ultra-long haul communications links [3]. Also, it shows that the CO-OFDM system could provide a feasible solution to the mitigation of Polarization Mode Dispersion (PMD) in existing installed fiber links [4,5].

The simulation was done by an advanced optical communications system simulation package designed for professional engineering called VPIphotonics simulating software by VPIsystems. VPIphotonics, represents an optical communications system as an interconnected set of blocks. Each block is simulated independently using the parameters specified by the user for that block and the signal information passed into it from other blocks [6].

This paper discusses coherent optical OFDM communications system, gives overview on coherent detection and shows that detection without using optical or electrical Phase Locked Loop (PLL) is possible. As well, details of proposed communications system are explained and explanation of simulation of CO-OFDM system and some simulation results of the CO-OFDM system are presented.

2. Coherent Detection

The most advanced detection method is coherent detection, where the receiver computes decision variables based on the recovery of the full electric field, which contains both amplitude and phase information. Coherent detection thus allows the greatest flexibility in modulation formats, as information can be encoded in amplitude and phase, or alternatively in both in-phase (I) and quadrature (Q) components of a carrier. At the receiving end, the receiver first adds a locally generated optical wave to the incoming information-bearing signal and then detects the combination. Coherent detection requires the receiver to have knowledge of the carrier phase, as the received signal is demodulated by a local oscillator (LO) that serves as an absolute phase reference. There are two basic demodulation formats, depending on how the signal is mixed with the local oscillator

which gives heterodyne or homodyne detection [7].

The received signal is detected either synchronously or asynchronously. The synchronous detection is more sensitive than asynchronous detection therefore it used in good coherent optical detection. Traditionally, carrier synchronization has been performed by a phase-locked loop (PLL). Optical systems can use one of the following ways:

(i) An optical PLL (OPLL) that synchronizes the frequency and phase of the LO laser with the TX laser.

(ii) An electrical PLL where down-conversion using a free-running LO laser is followed by a second stage demodulation by an analog or digital electrical VCO whose frequency and phase are synchronized.

PLL's are sensitive to propagation delay in the feedback path, and the delay requirement can be difficult to satisfy. The principle of polarization insensitivity for CO-OFDM system use Feed-forward (FF) carrier synchronization overcomes the propagation delay problem [4]. In addition, as a FF synchronizer uses both past and future symbols to estimate the carrier phase, it can achieve better performance than a PLL which, as a feedback system, can only employ past symbols.

3. CO-OFDM Transmission System

A coherent CO-OFDM transmission system is shown in Fig. (1). At the transmitter, the OFDM symbol is generated as follows: NQAM input QAM symbols are zero-padded to obtain NFFT input samples for inverse FFT (IFFT), NG non-zero samples are inserted to create the guard interval, and the OFDM symbol is multiplied by the window function [8]. Two Mach- Zehnder modulators (MZMs) encode the RF OFDM signal onto an optical carrier and perform pulse shaping. Two MZMs are needed, one for each polarization (I and Q). The laser diode output is used as a CW source is split into two orthogonal polarization components, which are modulated separately and combined in a polarization beam splitter (PBS). Also, it can be added modulation format (e. g. NRZ or RZ) to the optical signal for increase the sensitivity of receiver.

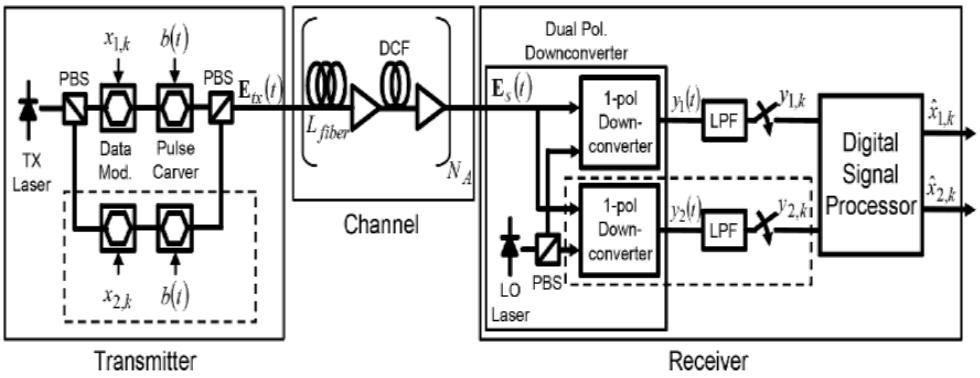

Fig. (1) Coherent transmission system

The first stage of a coherent receiver is a dual-polarization optoelectronic down-converter that recovers the base-band modulated signal. A dual-polarization down-converter is shown inside the receiver of Fig. (1). The output of a local oscillator laser must be added to the received signal with an identical polarization before photo-detection; alternatively, a polarization diversity receiver can be used [9]. The local oscillator (LO) laser is polarized at 45° relative to the polarized beam split (PBS), and the received signal is separately demodulated by each LO component using two single-polarization down-converters in parallel. The four outputs are the I and Q of the two polarizations, which has the full information of electrical field of optical signal at end of fiber $E_s(t)$.

A single-polarization down-converter, involve the LO laser is aligned in the certain polarization. Down-conversion from optical pass-band to electrical base-band can be achieved either by a homodyne or by a heterodyne receiver. In case of the heterodyne receiver, the local oscillator and transmitter (TX) lasers differ by an intermediate frequency (IF), and an electrical LO is used to down-convert the IF signal to base-band.

4. Simulation Analysis for CO-OFD System

The experiment setup is illustrated in Fig. (2). This system is simulated by using VPIphotonic simulation software. The experimental setup of CO-OFDM system uses direct up/down conversion architecture and intermediate frequency (IF) architecture. This setup can operate either on direct up/down conversion architecture or direct up/IF down-conversion architecture by select the analog switch in clock

either to clock recovery or to electrical local oscillator.

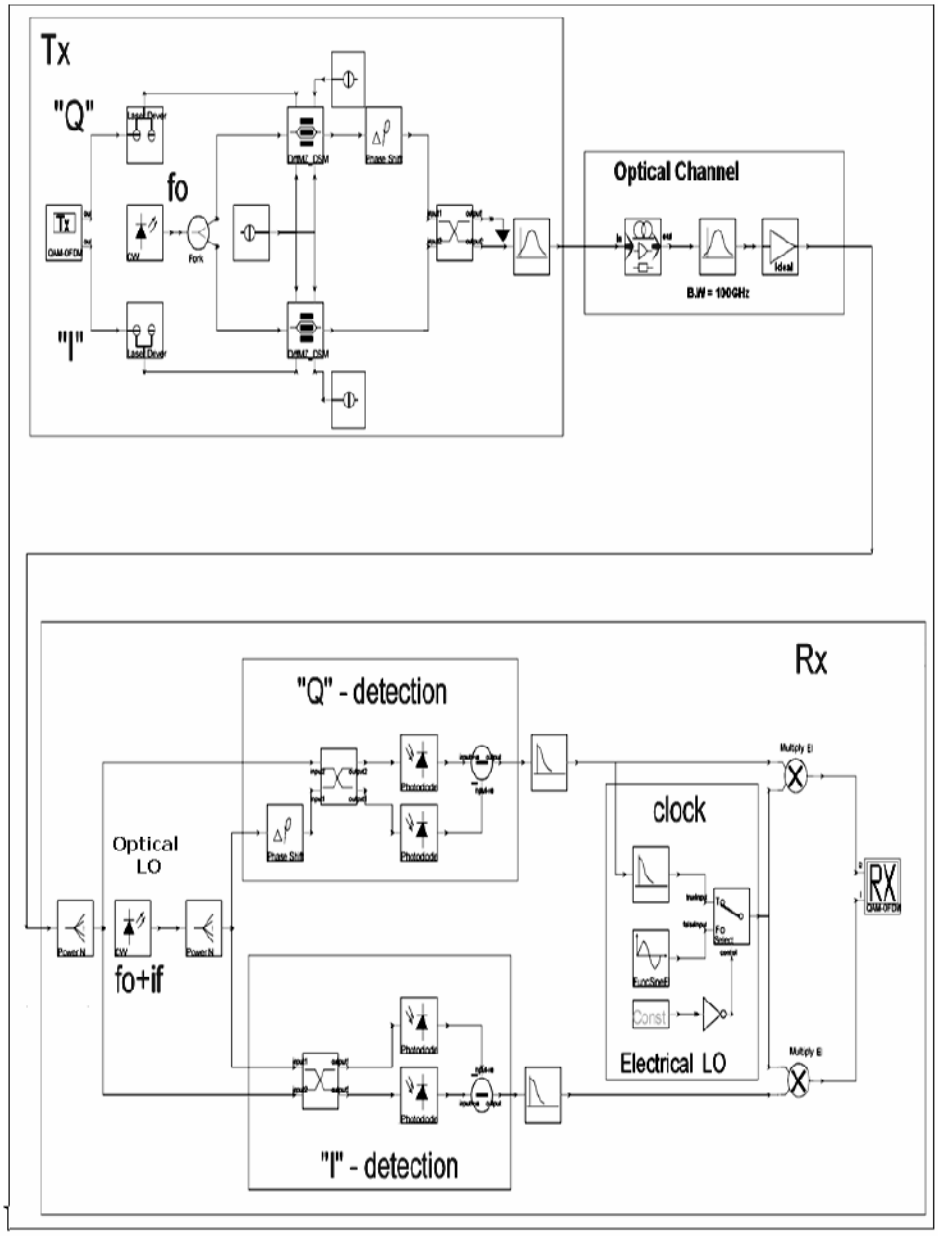

Fig. (2) The experiment setup of CO-OFDM communication system

In the direct up-conversion architecture, the optical transmitter consists of QAM-OFDM transmitter with I and Q signals and modulation format of NRZ, CW laser with optical frequency (f_o) as optical source, two Mach-Zender modulators (MZM's) to up-convert the real/imaginary parts of the QAM-OFDM transmitter, from the RF domain to the optical domain, i.e., each MZM is respectively driven by the real or imaginary part of the transmitter signal, and fiber couplers to recombine outputs of two MZM's and lunched to the optical channel.

The carver is not shown in OFDM system because it represents pulse shape or modulation format (e.g, NRZ or RZ). In this simulation, the modulation format is set inside TX of (QAM-OFDM) to NRZ modulation format. The transmitted signal can be written as:

$$E_{tx}(t) = \begin{bmatrix} E_{tx,1}(t) \\ E_{tx,2}(t) \end{bmatrix} = \sqrt{P_t} \sum_k x_k b(t - kT_s) e^{j(\omega_s t + \phi_s(t))} \quad (1)$$

where T_s is the symbol period, P_t is the average transmitted power, $b(t)$ is the pulse shape (e.g., non-return-to-zero (NRZ) or return-to-zero (RZ)), ω_s and $\phi_s(t)$ are the frequency and phase noise of the TX laser, and $x_k=[x_{1,2},x_{2,k}]^T$ is a 2×1

complex vector representing the *k*-th transmitted symbol.

In the direct down-conversion (homodyne) architecture, the OFDM optical receiver involves dual-polarization optoelectronic down-converter uses two pairs of balanced receivers and an optical 90° hybrid to perform optical I/Q detection. The RF OFDM receiver performs OFDM base-band processing to recover the data. The advantages for such direct-conversion architecture are (i) no need for image rejection filter in both transmitter and receiver, and (ii) significant reduction of the required electrical bandwidth for both transmitter and receiver [10].

In the IF down-conversion system (heterodyne), the optical OFDM signal is first down-converted to an intermediate frequency IF and the electrical I/Q detection is performed. The heterodyne receiver involves dual-polarization optoelectronic down-converter, CW local oscillator laser running with optical frequency (f_o +IF), electric LO used for down-conversion of the IF signal to base band. In a coherent receiver, a local oscillator (LO) is required to down-convert the received signal. In general, the LO will have random phase fluctuations relative to the transmitter oscillator. The distortion due to transmitter laser and receiver LO phase noise will then appear as a random rotation of points in the received constellation [11].

Optical channel involves the optical fiber and optical amplifier. Optical signal-to-noise ratio (OSNR) can be set from 20dB to 50dB by adding amplifier spontaneous emitting (ASE) noise to the optical signal.

Zero-padding encoding is used to generate the OFDM signal, so that the clock signal and modulated signal do not overlap in frequency as shown in Fig. (3). It was shown that in the noiseless case with ZP-OFDM, the transmit symbol can be recovered regardless of the channel zero locations [12].

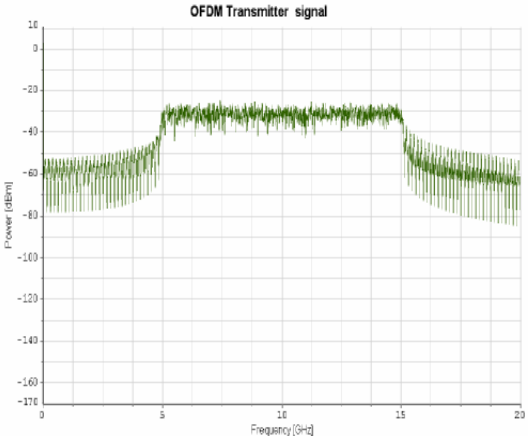

Fig. (3) Zero-padding OFDM transmitter signal

One of the parameters governing performance is the laser source linewidth. For different laser and LO linewidth (LW) values (10^5, 10^6 and 10^7) Hz, clock (eye diagram of receive signal) can be observed as shown in Fig. (4). The influence of laser and LO linewidth on the received constellation diagram is shown in Fig. (5). This test was performed under OSNR of 35dB and laser driver bias of 0.03.

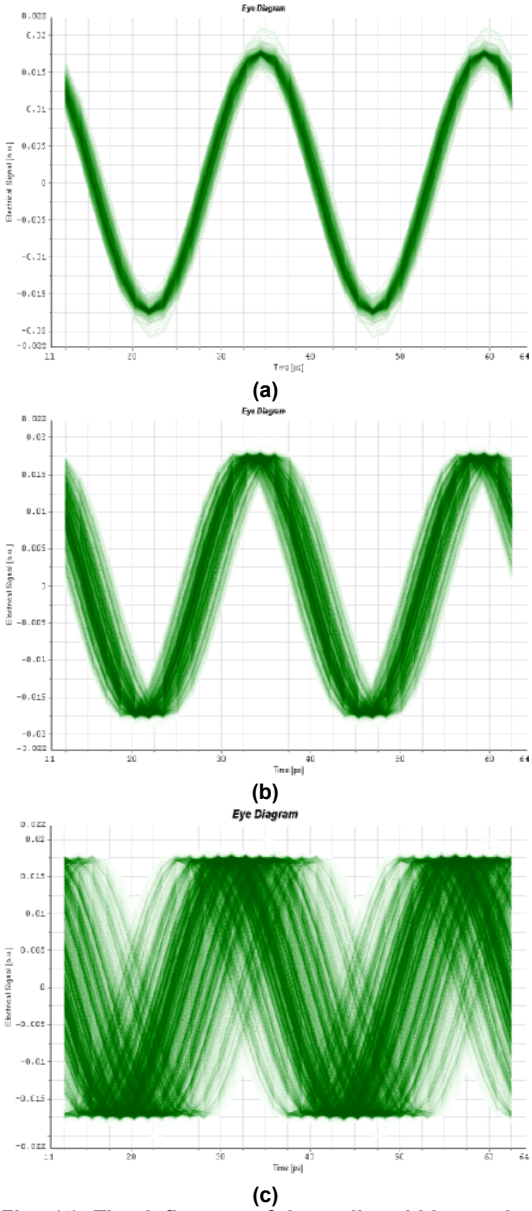

Fig. (4) The Influence of laser linewidth on the received eye diagram (a) LW=10^5Hz, (b) LW=10^6Hz, (c) LW=10^7Hz

The clock information (phase and frequency mismatch between transmitter and receiver) is contained in the "laser LO" beat term that is extracted at the receiver using an electrical filter and used for down-conversion and phase correction.

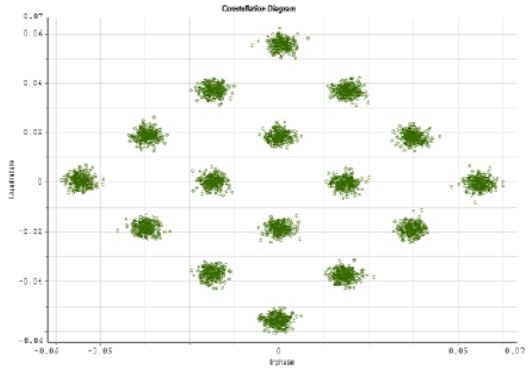

(a)

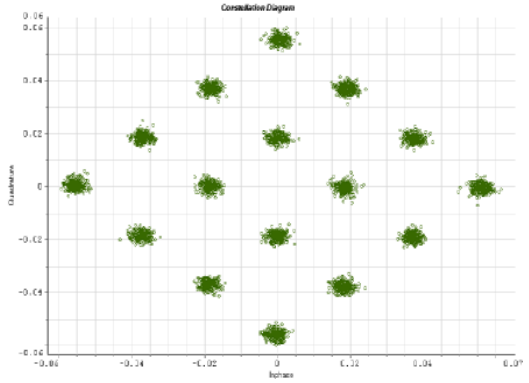

(b)

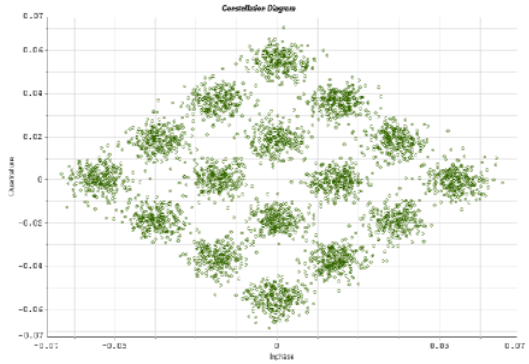

(c)

Fig. (5) The influence of laser and LO linewidth on the received constellation diagram (a) LW=10^5Hz, (b) LW=10^6Hz, (c) LW=10^7Hz

The performance of the proposed method depends on the strength of the extracted clock signal, which can be tuned by dividing the In-phase (I) and Quadrature (Q) MZM's slightly asymmetrical, i.e., the MZM is slightly biased. Therefore, the eye-diagram and the constellation diagram are the best with bias of 0.05V and they become worst with bias of 0 and 0.1V, as shown in Fig. (6).

The optical ASE noise is modeled as white Gaussian noise, and laser phase noise is assumed to be white frequency noise. The influence of phase noise in OFDM systems is two-fold, i.e., it generates a common phase rotation of all the sub-carriers in one symbol and a cross-leakage between the sub-carriers named inter-carrier interference (ICI).

The receiver performance of CO-OFDM system with influence of noise is shown in Fig. (7), in which, the experiment system is tested with OSNR of 20dB, 35dB and 50dB, respectively. The effect of OSNR on the optical spectrum, constellation diagram and clock signal is plotted. The influence increasing of OSNR on the received optical spectrum is making the noise level under -47dB. Also, the constellation diagram becomes clearer with increasing OSNR because the strength of the extracted clock signal becomes high. Figure (8) illustrates the relation between the BER and the laser source linewidth at OSNR of 25dB and 35dB. For OSNR of 25dB, lower BER (10^{-5}) at laser linewidth of 10kHz. The BER increased slightly for linewidth of 100kHz and it became very high with 10MHz and the system failed to detect optical signal. For OSNR of 35dB, lower BER of $2x10^{-6}$ at laser linewidth of 10kHz. The BER increased slightly for linewidth of 100kHz and reached to 10^{-4} for linewidth of 10MHz and the system still at suitable operation.

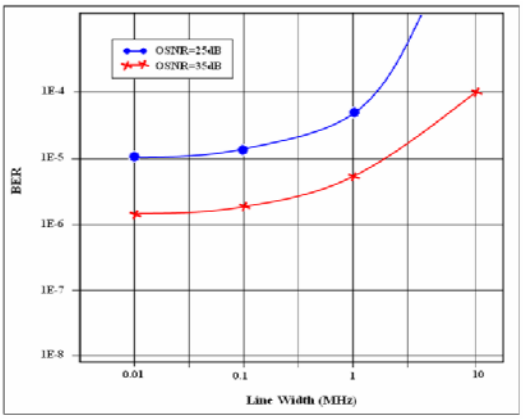

Fig. (8) Relation of laser source linewidth with BER at different OSNR

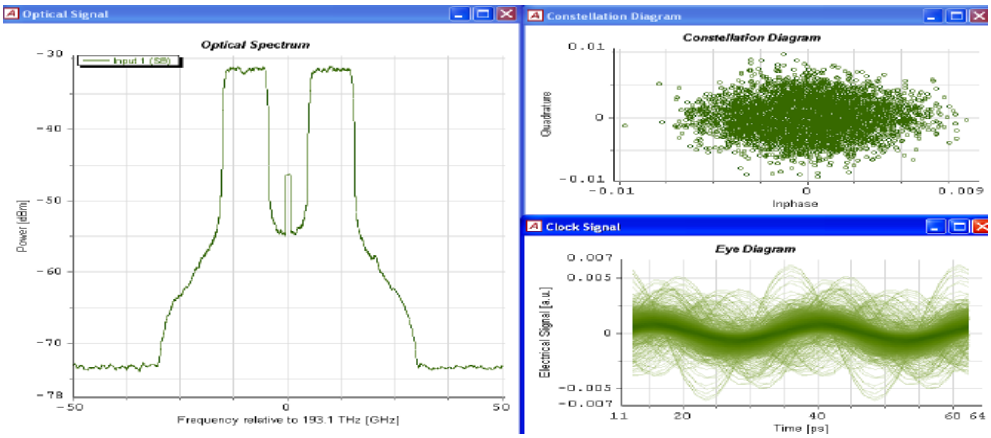

(a)

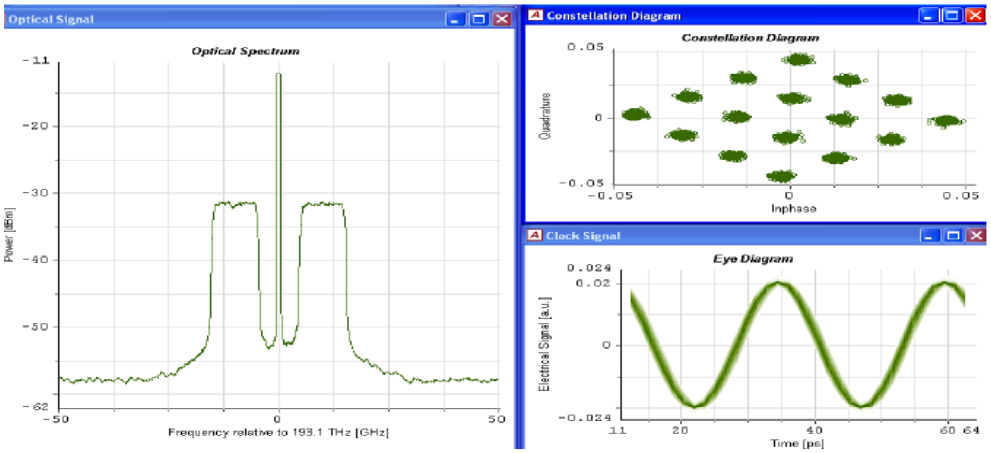

(b)

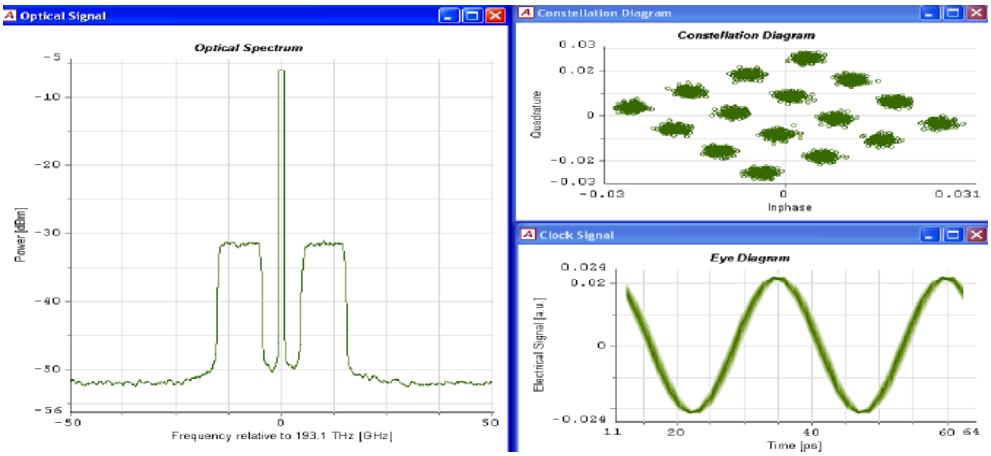

(c)

Fig. (6) The effect of changing MZM bias on the receiver performance at bias of (a) 0, (b) 0.05V, and (c) 0.1V

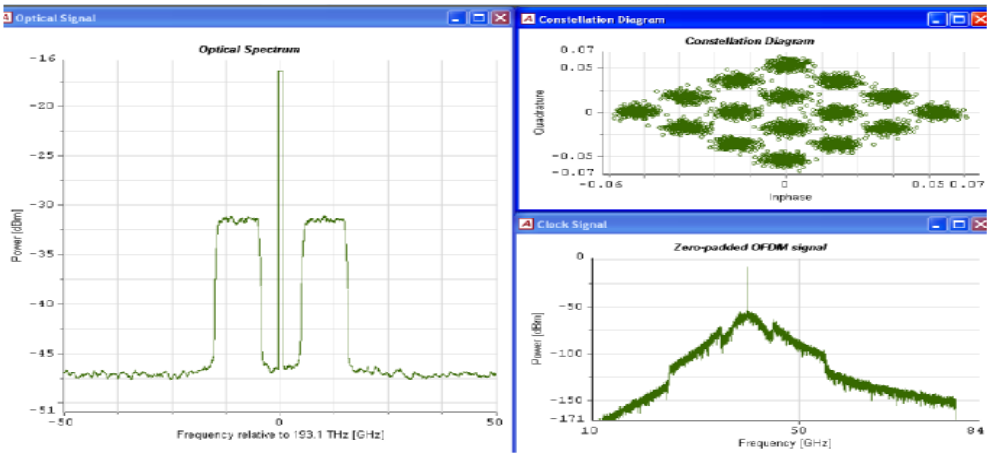

(a)

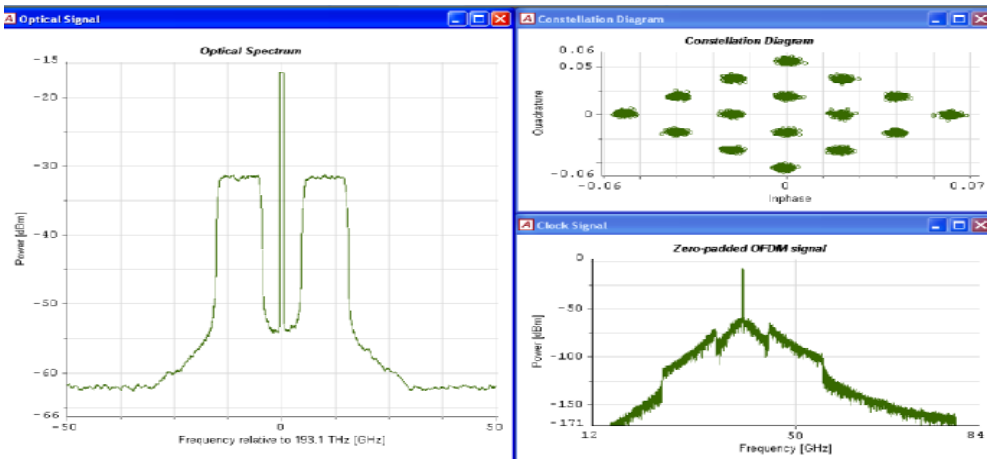

(b)

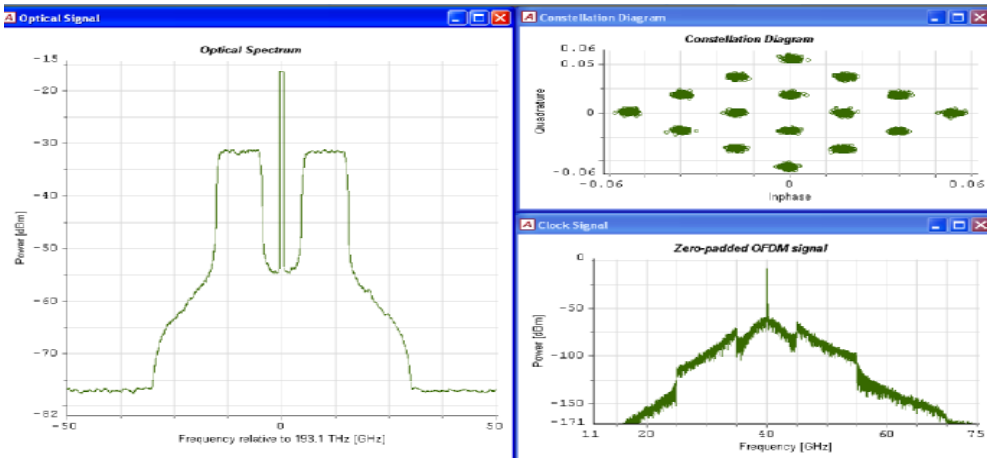

(c)

Fig. (7) The influence of noise on the optical spectrum, received spectrum and constellation diagram at OSNR of (a) 20dB, (b) 35dB, and (c) 50dB

5. Conclusion

This paper reports and depicts the results of using CO-OFDM telecommunications system in high bit rate optical transmission systems. The drive for higher performance in optical fiber systems can be achieved by coherent detection. The dual-polarization heterodyne down-conversion is linear process that can fully recover the received signal field. The coherent heterodyne detection of high bit rate OFDM signals without electric or optical-locked loop (PLL) was studied. The analytical study was employing standard optical fibers. The laser linewidth had an effect on the optical

ISSN 1813-2065

communications system; therefore, the laser linewidth must be set to approximately 10^6Hz for suitable performance. The suitable system performance obtained by slightly tuning I and Q MZM's to bias of 0.05V.

References

[1] A. Ahmad, **"Wireless and Mobile Data Networks"**, John Wiley & Sons, Inc. (2005), Ch.4, 76.

[2] W. Shieh and C. Athaudage, *IEE Proc. Electron. Lett.*, 42 (2006) 587-588.

[3] A.J. Lowery and J. Armstrong, *Optics Express*, 14(6) (2006) 2079-2084.

[4] W. Shieh, W. Chen and R.S. Tucker, *IEE Proc. Electron. Lett.*, 42 (2006) 996-997.

[5] S.L. Jansen et al., "Optical OFDM - A Candidate for Future Long-Haul Optical Transmission Systems", Optical Fiber communication/National Fiber Optic Engineers Conference, 2008. OFC/NFOEC 2008, 24-28 Feb. (2008) 1-3.

[6] VPIsystems Inc. "Photonic Design Automation, Expert Solutions for Optical Equipment Design".

[7] G. Keiser, **"Optical Fiber Communications"**, 2nd ed., McGraw-Hill (1991) 379-380.

[8] I.B. Djordjevic, L. Xu, and T. Wang, *Optics Express*, 16(19) (2008) 14845-14852.

[9] W. Shieh, H. Bao, and Y. Tang, "Coherent optical OFDM: theory and design", *Optics Express*, 16(2) (2008) 841-859.

[10] A.J. Lowery, S. Wang and M. Premaratne, *Optics Express*, 15(20) (2007) 13282-13287.

[11] A.H. Sayed et al., *Lightwave Technol.*, 24(3) (2006) 1269-1276.

[12] S. Pfletschinger and F. Sanzi, "Iterative Demapping for OFDM with Zero Padding or Cyclic Prefix", IEEE Int. Conf. on Communication (ICC), Paris (2004), 842-846.

MNC 2009

22nd International Microprocesses and Nanotechnology Conference

November 16-19, 2009

Conference Site:
Sheraton Sapporo Hotel, Sapporo, Japan

MNC 2009 SCOPE and SYMPOSIUM
1-1: DUV, EUV Lithography and Metrology
1-2: Electron- and Ion-Beam Lithography
1-3: Resist Materials and Processing
2-1: Nanodevices
2-2: Nanofabrication
2-3: Nanomaterials
2-4: Nano-Tool
3: Nanoimprint, Nanoprint and Rising Lithography
4: Bio MEMS, Lab on a Chip
5: Microsystem Technology and MEMS
Symposium A. Computational Lithography
Symosium B. Graphene: Growth & Characterization
Sponsored by
The Japan Applied Physics Physics

Committee Chairs:
Organizing Committee Chair:
S. Shoji (Waseda Univ.)
Steering Committee Chair:
T. Itani (Selete)
Program Committee Chari:
T. Meguro (Tokyo Univ. of Sci.)

Sponsored by
The Japan Society of Applied Physics

Cooperation
Association of Super-Advanced Electronics Technologies
The Institute of Electrical Engineers of Japan
The Institute of Electronics, Information and Communication Engineers
The Japan Society for Precision Engineering
The Japanese Society for Synchrotron Radiation Research
The Japanese Society of Electron Microscopy
The Surface Science Society of Japan
The Vacuum Society of Japan

MNC 2009 SCOPE and SYMPOSIUM

1-1:DUV, EUV Lithography and Metrology
This session focuses on DUV, EUV, Immersion Lithography, and Computational Lithography including OPC, SMO, DFM. In addition, Metrology such as SEM and Scatterometry is included.

1-2:Electron- and Ion-Beam Lithography
Electron and ion beam technologies such as lithography, metrology, inspection and repair tools. Other related technologies using charged particle beams are also welcome.

1-3:Resist Materials and Processing
Resist materials(EUV, immersion, double patterning,

DUV, EB, X-ray, multilayer, inorganic, molecular glass etc.), antireflective coatings, polyimide, adhesive, and other materials related to lithography. resist processes (PEB, development, rinse, resist removal, etching etc.)characterization, line edge roughness, trade-off problem, outgassing, modeling and simulation of resist process (exposure, acid diffusion, development etc.). materials and processes for the production of flat-panel display, photonics devices, and electronics packaging.

2-1:Nanodevices
Nanodevices and related technologies targeting more Moore, more than Moore and beyond CMOS; next-generation Si and compound semi conductor-based FETs, graphene FETs, 1D FETs such as nanowire FETs and carbon nanotube FETs, quantum dot devices, and all other nanodevices utilizing nanostructures and nanomaterials such as inorganics, organics, and molecules. Novel-concept devices utilizing nanostructures and nanophysics are also welcome.

2-2:Nanofabrication
Fabrication of nanostructures. Fabrication techniques such as scanning probe techniques, self-organizing techniques, etc. Physics and chemistry in nanofabrication processes. Etching, deposition, and related subsurface processing using photon, electron- and ion-beams, plasma, and thermal energy. Emerging technologies are also welcome.

2-3:Nanomaterials
Theory, properties, characterization and application of nanomaterials such as quantum dots, nano-particles, nanowires, carbon nanotubes, fullerenes, organic, molecular, and biomaterials. Materials prepared by self-organized or bottom-up approach are also included.

2-4:Nano-Tool
Nano-electromechanical system (NEMS), Nano-mechanics, Nanometrology, Metrology and repair for nanosystem, Novel observation and fabrication methods based on microscopic techniques, such as scanning probe microscopy (SPM), scanning electron microscopy (SEM) and focused ion beam (FIB).

3:Nanoimprint, Nanoprint and Rising Lithography
This session focuses nanoimprint system, process, material, applications and related inspection and metrology. Other novel nano-patterning technologies are also included. This session focuses nanoimprint system, process, material,applications and related inspection and metrology. Other novel patterning technologies are also included.

4:Bio MEMS, Lab on a Chip
Micro/nano electromechanical devices (M/NEMS) are now widely applied to biochemical, medical and environmental fields and a new research field called μ-TAS or Lab. on a Chip is expanding. Fusion of microelectronic devices with materials and methods in the biomedical fields is expected to open up new scientific and business areas. Papers are solicited in the following areas (but not limited): (1) MEMS/NEMS devices for biomedical fields, (2) μ-TAS and Lab on a chip, (3) Bio-chips for DNA, proteins and cells, (4) Fabrication technologies.

5:Microsystem Technology and MEMS
Fabrication techniques, design, mechanical characterization of three dimensional microstructures, and their applications to micromechanical systems, which include microwave and photonics devices, vacuum microelectronics, novel sensors and actuators, etc.

Symposium A. Computational Lithography
Symosium B. Graphene: growth & characterization

PLENARY SPEAKERS
S. Wurm (SEMATECH) A. Neureuter (Univ. of CA)
INVITED SPEAKERS
DUV, EUV Lithography and Metrology Session **T. Uchiyama (NEC Electronics)** Electron and Ion Beam Lithography Session **H. Loeschner (IMS Nanofabrication)** Resist Materials and Processing Session **M. Shirai (Osaka Pref. Univ.)** Nanodevice Session **Y.-M. Lin (IBM)** Nanofabrication Session **T. Fukui (Hokkaido Univ.)** Nanomaterials Session **Y. Einaga (Keio Univ.) I. Suemune (Hokkaido Univ.)** Nano-Tool Session **T. Funatsu (Univ. of Tokyo)** Nanoimprint, Nanoprint and Rising Lithography Session **H. Schift (Paul Scherrer Inst.) Q. Xia (HP)** Bio MEMS, Lab on a Chip Session Microsystem Technology and MEMS Session Symposium A. Computational Lithography **K. Lai (IBM) A. Erdmann (Fraunhofer) T. Matsuyama (Nikon) T. Takigawa (Brion Technologies) L. Pang (Luminescent Technologies) M. D. Smith (KLA-Tencor) W. Demmerle (Synopsys)**

Abstract Deadline: June 30 2009.

Late News Paper Deadline (2nd Abstract Deadline): September 15, 2009

Technical Seminar in Japanese is sponsored by Hokkaido Univ.

CONTACT US:
Secretariat for 22nd International Microprocesses and Nanotechnology Conference (MNC 2009)
c/o Secretaryart Corporation
TEL:+81-3-5367-1735
FAX:+81-3-5367-1736
Email: secretariat@imnc.jp

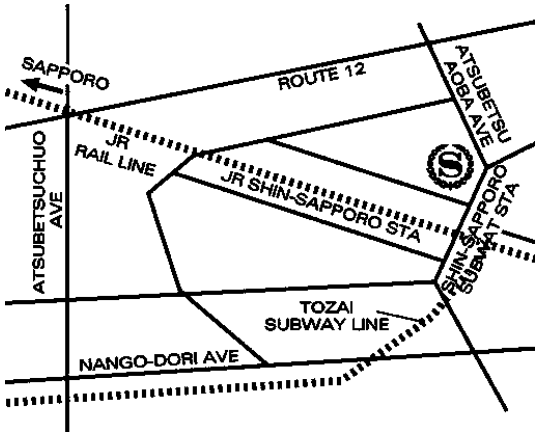

Global Warming

by Kevin E. Trenberth
National Center for Atmospheric Research
Climate Analysis Section, Colorado, USA

There was nothing profound that led me to my current career. Although I am a climate scientist with primary training in atmospheric sciences, neither weather nor climate were passions of mine as a youth. However, I was fortunate to be adept in mathematics, and my undergraduate work led me to a First Class honours degree in Mathematics at the University of Canterbury in New Zealand, where I was raised. In seeking employment, I was attracted to meteorology primarily through the link with fluid dynamics, which I had studied earlier. A key advantage of employment in the New Zealand Meteorological Service at that time was training in diverse aspects of meteorology as a prelude to working as a junior weather forecaster (shift work!). This was prior to my winning a New Zealand Research Fellowship to study overseas (at the Massachusetts Institute of Technology), where I was able to further diversify my background with theory and modeling. Following my doctorate, I returned to New Zealand for nearly seven years before moving to United States; a consequence in part of having married an American girl.

A great deal of my research has focused on regimes, or persistent patterns of variability, in weather and climate. This interest stemmed from the early part of my career in New Zealand, where I observed as a forecaster what appeared to be weather patterns that lasted for more than a season. Subsequently these patterns have been linked in part to the El Niño phenomenon, partially through my own work. The cited work was an attempt to provide as comprehensive analysis of the observational record as possible on time scales from days to multi-decadal, with a focus on North Pacific variability and links to El Niño. This work therefore enabled the documentation of how storm tracks change as the atmospheric circulation changes in this region, and it identified multi-decadal climate variations that are of considerable importance and which may well be linked to climate change, and specifically to global warming. It further identified the effects of these variations on rainfall, temperatures, the ocean, and such things as the salmon harvest.

Our recent work has raised questions about how El Niño will change as climate changes, and detailed statistical and diagnostic analysis has provided a good basis for believing that there is a relationship. We have also documented more comprehensively how El Niño itself evolves in various manifestations (wind, temperature, atmospheric circulation, cloud, radiation, precipitation, storminess, movement of heat and energy, exchanges of heat and moisture with the surface) throughout its life cycle, and how that evolution appeared to change abruptly around about 1976-77, as was first partly outlined in the cited article. This has subsequently become well recognized as the 1976-77 climate shift. We have also recently documented El Niño relationships to global mean temperature and how it is manifested through the local surface temperatures all over the globe.

How El Niño changes as climate changes and global warming progresses is a critical question of great importance for many regions of the globe. While our exploratory analyses are suggestive and form useful hypotheses for future work, climate models do not yet simulate El Niño well enough and are too different from each other to have any confidence in their projections. This itself is an indication of a lack of adequate understanding of some aspects of El Niño and its role in the global climate system. Accordingly, we continue to seek improved analyses of the past and associated diagnostic studies that will clarify the role of El Niño and improve its prediction. A focus for some of the research is quantitative diagnostic estimates of the energetics of El Niño, so that we can track how the heat builds up in the ocean and is subsequently redistributed and dissipated during the El Niño event. The underlying hypothesis is that El Niño exists and plays a role in the Pacific Ocean as a means of removing heat from the equatorial regions of the ocean, where it would otherwise build up. An implication of this, if correct, is that further heat buildup from increasing greenhouse gases in the atmosphere would lead to increased magnitudes and/or frequency of El Niño events. Nevertheless, we do not expect this to be simple, and nature always seems to be able to come up with surprises as to just what the future holds.

Mohammed S. Mehdi [1]
Maysam T. Al-Obaidi [2]

[1] *Department of Laser Engineering, University of Technology, Baghdad, Iraq*
[2] *Department of Physics, College of Sciences, Al-Mustansiriya University, Baghdad, Iraq*
may_obaidi@yahoo.com

Signal Mechanism Analysis of Fiber Arrival Time in Fiber Optic Pin

In this research there has been a description and studying for Fiber Arrival Time (FAT) technique. The research has depended on a theoretical analysis way for the FAT technique that is mainly used as a sensor and detector for the detonation waves (thermal waves) that is produced by high explosives. Several explanations for the output optical signal in FAT diagnostic have been introduced, the suggested by previous researches as well as the suggested by this research. Wien's displacement law has been depended to measure the wavelength of the output optical signal. Also, heat measurements have been performed in this research and each of heat transfer coefficient and heat gradient in FAT diagnostic has been measured. There has been a comparison by using several other elements like copper, silver and gold as probable substitutes for aluminum that has been used in FAT.

Keywords: Rise time, Arrival time, Denotation waves, *Al* transmission
Received: 13 March 2009, **Revised**: 10 May 2009, **Accepted**: 17 May 2009

1. Introduction

Recently, there has been a great demand for an accurate and practical methods for measuring what we call the dead/break out time of waves particularly detonation waves resulting from high detonation cases, knowing that the intrinsic rise time for the signal generated in such high detonation is less than one-nanosecond.

Many researches have been published in the field of rise-time (response time) calculation, one of these researches has provided us with an interesting technique which is known as Fiber Arrival Time (FAT) technique. The aim of this technique is to detect the detonation waves within short response time and hence get better time resolution than the available techniques, depending on a fiber optic pin of sufficient time resolution and relatively inexpensive. This type of techniques is so important in the military fields, many studies for the Navy have been introduced in order to understand the signal generation by using the technique of (FAT) in order to improve the response time for the detonation waves [1,2].

Many conclusions of the Navy study have been depended in our research, which will try to introduce the main mechanism of the output signal that produced by high explosives and detected by using (FAT) diagnostic.

2. Description of the FAT Diagnostic

The FAT technique consists of an optical fiber of 100μm in diameter centered with ±10μm which is chemical vapor deposition (CVD). The end of this fiber is coated with (1200-1500)Å of *Al* element and this coating thickness was chosen according to time-response desired and the transmission curve of *Al* for visible light.

The coating thickness of the optical fiber must be at least in the range of ~500Å, in order to avoid the unwanted light transmissions which generated within the explosive and that could be detected with the intrinsic signal. The idea of the FAT technique depends on the interaction between the detonation wave and the surface of the aluminum coat which will cause an intense, fast rise-time pulse of light that will be collected by an optical fiber and transmitted to an optical detector (electronic streak camera/CCD readout). The output was recorded on a film which is a deposited *Al* film of 2.5 gm/cm^3 as a thickness. Several high explosives have been used in this diagnostic: LX-16 (96% PETN), LX-14 (95.5% HMX), HMX, RDX, RX-08-HD (73.6% HMX and 19.9% TMETN). Figure (1) shows a schematic of the FAT diagnostic [1].

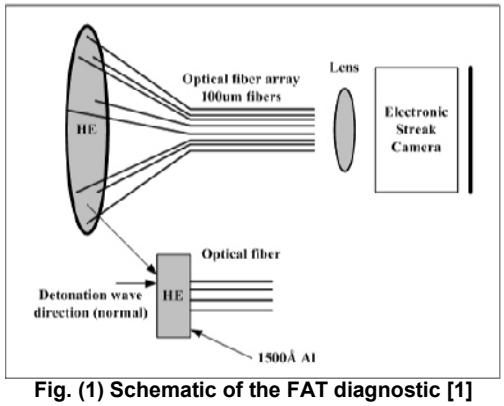

Fig. (1) Schematic of the FAT diagnostic [1]

In our research there will be a type of theoretical analysis for the generated signal in the technique of FAT and the most probable explanations as to cause this optical signal.

The main reasons that have been mentioned in the published research of the FAT were in briefly [3]:

1) Sudden change in the transmission properties of the *Al*.
2) Thermal diffusivity from the hot high temperature reaction products.
3) Aluminum combustion with the reaction products. [The last two points (reasons) are referred to the Aluminum film that have been used in this technique].
4) A combination of the above factors.

It's important to mention here, that we'll also try to use other chemical elements in the composition of this technique instead of *Al* depending on thermal properties like thermal conductivity, diffusivity and diffusion time.

3. Heat Transfer Mechanism

At first in this part we shall try to determine the type of heat transfer mechanism in the mentioned technique. In general, the heat transfer mechanisms are conduction, convection, radiation (thermal radiation) and other heat transfer mechanism.

In this research, since we have detonation waves and optical signal, then the heat transfer mechanism is the thermal radiation. And we should mention that the thermal radiation is a direct result of movements of atoms and molecules in the material. Since these atoms and molecules are composed of charged particles (electrons and protons), their movements result in the emission of electro-magnetic radiation which carries energy a way from the surface of the high explosive material (black body) [4,5], so we consider that the electro-magnetic radiation is the first step behind the generation of the output optical signal.

For any given temperature of the electromagnetic radiation, there is a frequency f_{max} at which the power emitted is a maximum. Wien's displacement law and the fact that the frequency of light is inversely proportional to it's wavelength in vacuum, mean that the peak frequency f_{max} is proportional to the absolute temperature of the black body [4,5]. In the next section Wien's displacement law will be used in order to measure the wavelength of the output optical signal in FAT diagnostic.

4. Wien's Displacement Law and the Wavelength of the Electro-Magnetic Radiation

Wien's displacement law is a law of physics that states that there is an inverse relationship between the wavelength of the peak of the emission of a black-body and it is temperature:

$$\lambda_{\max} = \frac{b}{T} \qquad (1)$$

where $\lambda_{\max}$ is the peak wavelength in meter, T is the temperature (K), and b is the constant of the proportionality which is called Wien's displacement constant (~2.897×10^{-3}mK)

For optical wavelength, it is often more convenient to use nanometers in place of meters as a unit of measure (b=2.89×10^{6}nm.K) [6].

In this research, the high explosive material will be treated as a black-body and hence the electro-magnetic radiation (electro-magnetic emission) of the detonation should obey Wien's law, in other words, the black-body thermal emission will be a reference point for the thermal radiation and the generated signal in the FAT diagnostic.

Since the temperature of the thermal radiation of the high explosive is in the range of 3500-4300K [1], then the wavelength of the generated signal will be about 672nm as a maximum wavelength according to Eq. (1).

This result of course is absolutely fit the spectrum of the black-body and when we compare the wavelength that have been produced by using Wien's law (672nm) with the wavelength of the generated signal of the FAT technique as in Fig. (2), that has been introduced by [1,7], we can see that there is a relative difference in the peak of the wavelength of the generated signal.

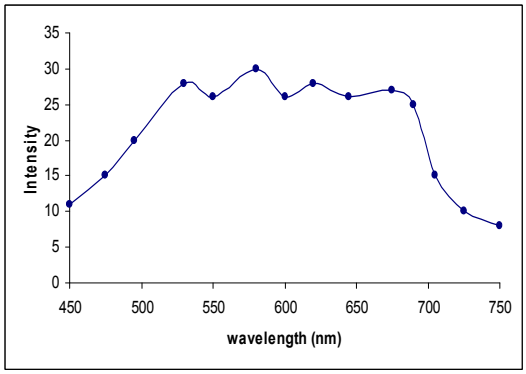

Fig. (2) Spectrum of intensity of signal as a function of wavelength in FAT [1]

The spectrum in Fig. (2) [1] shows several peaks which represent an increasing in the intensity rate in the range 580-670nm, and this spectrum supports the dependence of Wien's law to measure the wavelength of the generate signals.

However, we refer this difference in the max wavelength to the following reasons:

1) According to Wien's displacement law "the hotter an object is the shorter the wavelength", so by increasing the temperature there will be a

reduction in the wavelength [6]. This might explain the difference in the wavelength theoretically and practically.

2) The ionization energy that produced by the hot high temperature reaction, which will be discussed further below.

5. Heat Measurements

5.1 Heat Transfer Coefficient of FAT Diagnostic

In order to determine the quantity of heat that transfers/passes in unit time through unit area in FAT technique of a particular thickness, the following equation have been used [8]:

$$Heat\ transfer\ coefficient = \frac{k}{X} \qquad (2)$$

where k is thermal conductivity of Al ≈237 W/mK and X is the thickness of Al coating ≈1500Å

By applying Eq. (2), the heat transfer will be in the range of (1.58GW/m^{2}K) or equals to (1.58GJ/s).

5.2 Fourier's Equation (Law) to Measure the Quantity of Conduction of FAT Diagnostic

By using Fourier Law of conduction, the heat gradient (dq/dt) can be measured according to the following equation [8]:

$$H = \frac{dq}{dt} = kA\frac{dT}{X} = 50\text{kW} \qquad (3)$$

where H is the enthalpy of heat, dq/dt is the heat gradient and A is the cross section area (m)

6. Signal Generation Mechanism

In order to understand the mechanism of signal generation in FAT technique, we'll try to mention the main explanations as to cause the obtained optical signal in FAT diagnostic. According to a previous study for the Navy, it was concluded that the thickness of the fiber end coating increases the intensity of the generated signal (in a limited range 1200-1500Å).

Also according to a study by [1], it is highly probable that the Al film combustion enhances the optical signal observed in FAT measurement. Particularly that the last study has also shown that the Al coating which was in contact with the high explosive material (LX-14), (LX-16) was completely burnt during the detonation. There is another possibility, that is under a static pressure of 310kbar, the reflectivity of Al changes by about 40%, which will consequently change the transmission of Al by changing the band-gap, however this reason was not depended as a main reason for the change of the Al transmission [1,2].

The possibility that the thermal diffusivity and hence the diffusion time of the Al film, which was in the range of 0.08-0.1ns can be involved as an important reason for the generation of the optical signal, particularly that each of the rise-time and diffusion time is less than one ns [1]. However this reason could not give us the main explanation that caused the optical signal, particularly that the frequency that is corresponded to the diffusion time does not lie in the optical part of the electro-magnetic radiation, so diffusion time can not be the main reason as to cause the optical signal. From the available evidences we can briefly say that we have a high explosive material that has a detonation wave of:

- 3500-4300K as a temperature
- 310-330kbar as a static pressure
- Heat transfer coefficient of 1.58GW/m^{2}K
- Heat gradient (dq/dt) in the range of 50kW face to face with a sensitive fiber end coating of 1500Å as a thickness (see Fig. (3)).
- Time of less than a few tens of pico-second (10^{-12}s) for the detonation wave as to traverse the Al coating, in other words, we can call it shockwave-time.
- Thermal diffusion time of Al film in the range of less than 0.1ns according to the equation of the thermal diffusion time:

$$t_d = \frac{X^2}{\pi D} \qquad (4)$$

where t_d is thermal diffusion time, X is the thickness of Al films in the FAT diagnostic and D is the thermal diffusivity of Al film (m^2.s)

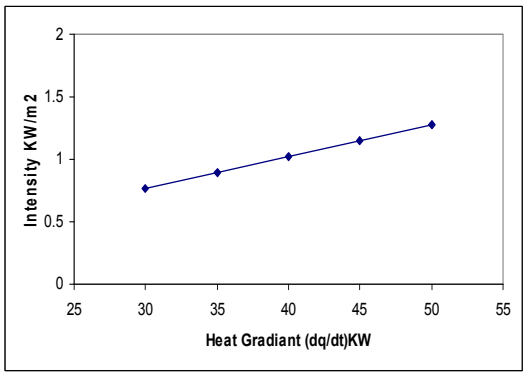

Fig. (3) The intensity of signal as a function of heat gradient

By comparing the shockwave-time (a few tens of pico-seconds) with the rise-time that was in the range of less than one nanosecond, we can estimate that there will be several reverberations through the time difference, this means that the Al coating has been put under a sever tension through this very limited time, (this point was mentioned by [1]).

Now by combining the above effective factors, it was concluded that the produced energy by the detonation will be sufficient enough to create an ionization energy that is proportional to the above factors and what might

support this conclusion is the quantity of heat transfer coefficient that was involved in this research (in the range of 1.6GJ/s).When we compare this enthalpy with the enthalpy that is required to produce the ionization energy for the *Al* (see Fig. (4)) which starts from the energy level of 577.5kJ as a 1st ionization energy reaching the energy level of 222315kJ for each mole as the 13th ionization energy (according to the atomic number of *Al*), we can estimate that the produced energy by heat transfer is well above the ionization energy of *Al* coat in the diagnostic of FAT.

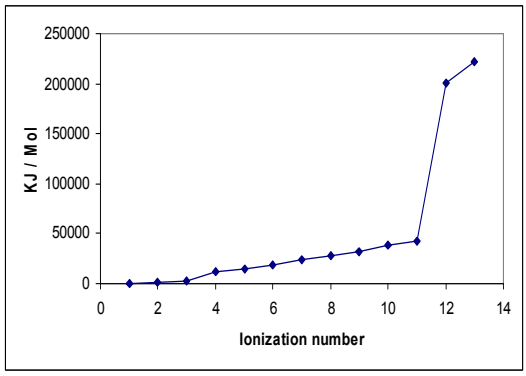

Fig. (4) The ionization energy of Al [9]

There is another point that might also support the suggestion of the ionization energy of the *Al* coat, which is the supposition that the *Al* combustion is enhancing the detected signals. This supposition was introduced by previous researches for the Navy [1,2].

In this research, figure (5) shows a type of comparison of the frequency in Hz of the generated signal as a function of the diffusion time in (nanosecond) of *Al* film and of several other elements (*Cu, Ag & Au*), which were supposed to have the same thickness of *Al* in FAT diagnostic (i.e., 1200-1500Å) [1].

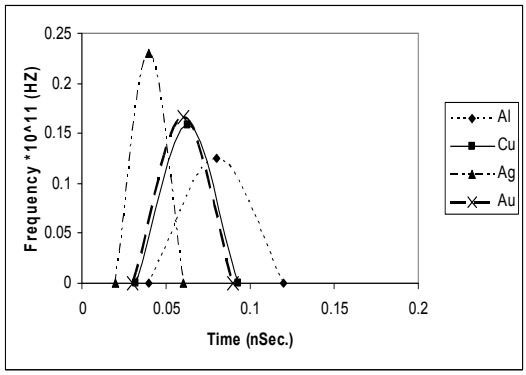

Fig. (5) The frequency of signal as a function of diffusion time

Figure (6) shows a comparison of diffusivity as a function of diffusion time of *Al* film in FAT diagnostic as well as of the same above elements. It's important to mention that these elements were chosen according to two main factors: thermal conductivity (*k*) and thermal diffusivity (*D*). Table (1) shows the data of this comparison [9].

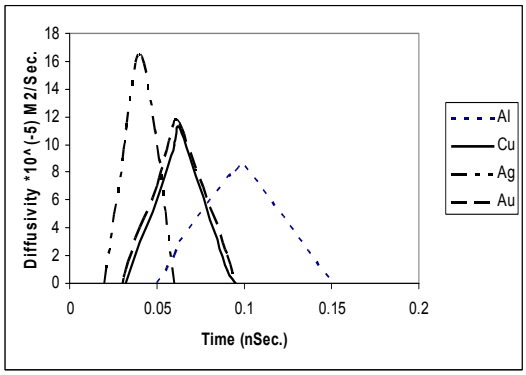

Fig. (6) The diffusivity as a function of diffusion time

Table (1) Elements thermal and diffusion values

Element	Thermal Conductivity (*k*) (W/mK)	Diffusivity (*D*) x10^{-5} m^2/s	Diffusion Time (ns)
Al	237	8.41	0.08 ≈ 0.1
Cu	401	11.23	0.063
Au	318	16.56	0.06
Ag	429	11.8	0.043

Also, since we have ionization energy in this diagnostic, then the atomic number can be depended to choose these elements.

7. Conclusion

The FAT diagnostic has been proved to be a highly useful, practical, inexpensive and reliable way that can be a substitutional technique for the detectors in order to measure the arrival time of the detonation waves of high explosives. We can conclude that because of the optical fiber that used in this technique, the FAT is highly used in difficult geometries cases, where direct optical imaging is difficult.

In this research several explanations as to cause the output optical signal have been introduced. The most probable explanation is the suggestion of the ionization energy of Al due to the high temperature, static pressure and short shock wave–time at the surface of Al coat. Via comparing figures in this research, we can estimate that substitution elements can be used in state of Al in FAT diagnostic, depending on several main factors like thermal conductivity, thermal diffusivity, diffusion time and atomic number of the element.

References

[1] F. Roeske, "Fast Rise-Time, Fiber Optic Pin", 11th Inter. Detonation Symp., Snowmass Village, CO, August 30-

September 4, 1998, Lawrence Livermore National Laboratory, May, (1998).
[2] R.F. Benjamin, F.J. Mayer and R.L. Maynard, *Proc. SPIE*, 506 (1984) 116.
[3] Y. Kato et al., "Temperature of Nitromethane and Some Solid High Explosives", 8th Int. Symp. on Detonation, Albuquerque, NM. July 15-19 (1985) 558-565.
[4] A.R. Moghadassi et al., *Brazil. J. Chem. Eng.*, 26(1) (2009) 199-206.
[5] B.R. J. Muhyedeen, *Euro. J. Sci. Res.*, 22(4) (2008) 584-601
[6] J. Mehra and H. Reachenberg, **"The Historical Development of Quantum Theory"**, Springer, Vol.6, Pt.1, Ch.1, (2001).
[7] A.M. Renlund and W. M. Troft, *J. de Physique Colloques*, 48(9) (1987) 179-188.
[8] I. Müller and W.H. Müller, **"Fundamentals of Thermodynamics and Applications"**, 2009 Springer-Verlag Berlin Heidelberg (2009) 179, 58.
[9] W. Callister Jr., **"Material Science and Engineering - An Introduction"**, 7th ed., John-Wiley & Sons, Inc. (2007) 910.

Latest Development

SOLAR ENERGY WILL DOMINATE BY 2030

Walid K. Hamoudi

Huge economic and technical gains were made by photovoltaics over the last 15 years. This gives confidence that a dramatic shift in electricity generation technology over the next quarter-century is possible. Progress in the proposed research could lead to: artificial "molecular machines" that turn sunlight into chemical fuel; "smart materials" based on nature's ability to transfer captured solar energy with no energy loss; self-repairing solar conversion systems; devices that absorb all the colors in the solar spectrum for energy conversion, not just a fraction; far more efficient solar cells created using nanotechnologies; and new materials for high-capacity, slow-release thermal storage. Revolutionary breakthroughs come only from basic research. We must understand the fundamental principles of solar energy conversion and develop new materials that exploit them. Cross-cutting research directions include: coaxing cheap materials to perform as well as expensive materials; developing new solar cell designs that surpass traditional efficiency limits; finding catalysts that enable inexpensive, efficient conversion of solar energy into chemical fuels; and developing materials for solar energy conversion infrastructure, such as transparent conductors and robust, inexpensive thermal management materials. All our buildings will feature energy-efficient design, construction, and materials as well as renewable energy technologies. In effect, each building will both conserve energy and produce its own supply, to be one of a new generation of cost-effective "zero-energy buildings" that have no net annual need for nonrenewable energy.

In photovoltaic research and development, there will be more breakthroughs in new materials, cell designs, and novel approaches to product development. In a solar future, the mode of transportation - and even the clothes we wear - could produce clean, safe electric power. With today's technology roadmaps to lead the way, concentrating solar power will be fully competitive with conventional power-generating technologies within a decade. Concentrating solar power, or solar thermal electricity, could harness enough of the sun's energy to provide large-scale, domestically secure, and environmentally friendly electricity, especially in the Arab countries. A desert area 10 miles by 15 miles could provide 20,000 megawatts of power. Within 10 years, photovoltaic power will be competitive in price with traditional sources of electricity.

Worldwide photovoltaic sales are growing at 40 to 50% per year. Research & market support for photovoltaics of around $400 billion spread over the next 25 years can deliver the technology required to eliminate electricity production as a contributor to climate change. Yet today solar electricity provides only approximately one thousandth of the total electricity supply. Sliver solar cell technology can achieve electricity costs below retail electricity costs within five years, with the right investment. Sliver cells are thin, single-crystal silicon solar cells fabricated using standard fabrication technology. Sliver modules, composed of several thousand individual Sliver cells, can be efficient, low-cost, bifacial, transparent, flexible, shadow tolerant, and lightweight. Compared with current PV technology, sliver solar cells use as little as one tenth the amount of hyper-pure silicon as in square solar PV technology, giving them the potential to produce electricity at grid-competitive prices.

Explosive growth in sales in the commercial and residential sector will then follow. It's not difficult to envisage Sliver based technology delivering electricity at a cost that matches wind energy, zero-emission coal and other clean energy technologies. No leap of faith is required; just careful engineering and adaptation of existing techniques from other industries. It is essential to eliminate carbon dioxide emissions from fossil fuel based electricity generation in order to limit climate change. The cost of doing this with advanced solar technology will be far lower than the pessimistic forecasts advanced by some analysts.

Photovoltaic energy has large potential in the Southern and Eastern Mediterranean as well as the Arabian gulf countries, especially where the electricity network covers only part of the country. Morocco is an example of such countries, as its electrification rate is very low and nearly 10.000 villages – with an average of 300.000 households still need electrification. The estimated potential of Morocco and Tunisia is respectively of 200.000 PV systems and 14.000 PV systems. Also Turkey has a high interest in the development of PV, with a special focus on water pumping, electric signals and telecommunications.

ISSN 1813-2065

IOP *Institute of Physics*
FORTHCOMING CONFERENCES

Plasma Surfaces and Thin Films
16 June 2009
The Institute of Physics, London, UK
Organised by the IOP Ion and Plasma Surfaces Interactions Group

Postgraduate Workshop on Magnetic Imaging
Wednesday 17 June 2009
University of Leeds, School of Physics and Astronomy
Organised by the Magnetism Group of the Institute of Physics
Co-sponsored by Royal Microscopy Society

Correlated Electron-Ion Dynamics: Debutante
13 July 2009
The Institute of Physics, London, UK

19th International Conference on Ion Beam Analysis
7 - 11 September 2009
University of Cambridge, UK
Organised by the IOP Ion and Plasma Surface Interactions Group

EMAG 2009 (including the Advanced School)
8 - 11 September 2009
University of Sheffield, UK
Organised by the IOP Electron Microscopy and Analysis Group

7th International Conference on Modern Practice in Stress and Vibration Analysis
8 - 10 September 2009
Organised by the New Hall, Cambridge, Stress and Vibration Group

Computer Simulation and the Environment
10 September 2009
Organised by the Institute of Physics, London, Computational Physics Group

Physical Aspects of Polymer Science (The 24th Biennial Meeting of the Polymer Physics Group of the Institute of Physics)
14 - 16 September 2009
Wills Hall, University of Bristol
Organised by the IOP Polymer Physics Group

Thin Film Photovotaics
16 September 2009
Institute of Physics, London, UK
Organised by the Ion and Plasma Surface Interactions Group

Sensors and their Application XV
5 - 7 October 2009
Heriot-Watt University, Edinburgh, UK
Organised by the IOP Instrument Science and Technology Group

Twentieth International Conference on Optical Fibre Sensors (ofs20.org)
5 - 9 October 2009
Edinburgh, UK
Organised by the IOP Optics and Photonics Division

Dynamics of Printed Drops - II
2 November 2009
Organised by: the Institute of Physics, London, Printing and Graphics Science Group

Low Temperature Techniques Course
4 November 2009
East Midlands Conference Centre
Organised by: the IOP Low Temperature Group

Experimental Techniques in Semiconductor Research
11 November 2009
East Midlands Conference Centre, Nottingham
Organised by: the IOP Semiconductor Physics Group

BRSG Christmas Meeting 2009
15 December 2009
Organised by: the Institute of Physics
BRSG: The Magnetic Resonance Group

Condensed Matter and Materials Physics (CMMP 09)
15 - 17 December 2009
Warwick University, UK
Organised by: the IOP Condensed Matter Division

T.J. Alward
K.R. Wissmiller
J.E. Knudsen *

Department of Electrical Engineering, Arizona State University, AZ 85287 USA
** jonathan.knudsen@asu.edu*

Power Reduction in Flexible Silicon Thin Film Digital Circuits

Amorphous silicon (a-Si) thin-film circuits promise robust, lightweight, flexible displays and digital computation. Here, several methods for reducing standby-power while retaining logic state are investigated for such circuits. Lacking a PMOS load transistor, the conventional approach for retaining state is to dynamically shift values through memory elements. We investigate other methods and demonstrate 36x power savings by introducing a non-shifting, refresh based operating mode.

Keywords: Power reduction, Thin films, Silicon devices, Digital circuits
Received: 27 January 2009, **Revised**: 11 February 2009, **Accepted**: 18 February 2009

1. Introduction

Amorphous silicon (a-Si) thin film transistors (TFT) on glass is the dominant technology for the active matrix backplane in flat panel displays [1], and digital radiography [2]. Recently, amorphous silicon thin film transistors have been fabricated on flexible substrates including plastic (Fig. 1) and stainless steel enabling a variety of new applications. Both reflective [3] and emissive [4] flexible displays have been built, and a small volume production facility for flexible a-Si backplanes is being established [5]. The flexible displays are lighter weight, more rugged, portable, and even wearable. Applications range from a soldier wearing a flexible display on a shirt sleeve receiving real time information to a tourist or hiker carrying an electronic roll out map. Even broader applications would be possible if digital computational electronics could be built in flexible a-Si TFTs. For instance, a flexible, disposable, electronic band-aid could monitor a patient's vital signs, perform the necessary digital computation and display the results.

There are several challenges with a-Si circuit design including low electron mobility, ranging from 0.1cm^2/Vs to 1cm^2/Vs. This mobility is 1000x less than that for single crystal silicon, making a-Si circuitry necessarily slow. Furthermore, only N-type amorphous silicon transistors are available, requiring dynamic NMOS circuit design techniques not widely practiced since the 1970's. And perhaps most challenging, the threshold voltage of a-Si TFTs increases significantly with electrical stress [6] posing a long term reliability problem. However, complex a-Si circuitry has been successfully designed on glass substrates for integrated row and column drivers for flat panel displays [7].

In this paper, we consider a portable, flexible digital electronic system in a-Si on plastic and determine the best approach to reduce power while saving the state of the digital machine. As a case study, we focus on a shift register as a fundamental building block of digital systems.

2. a-Si TFT Circuits

The flexible circuitry is realized using a-Si TFTs (Fig. 1). The substrate is thin plastic (heat stabilized PEN), allowing the circuits to be flexible. The gate electrode material is aluminum and spans the entire transistor on the bottom side. The gate dielectric is silicon nitride. All processing steps are below 150°C for compatibility with the plastic substrate.

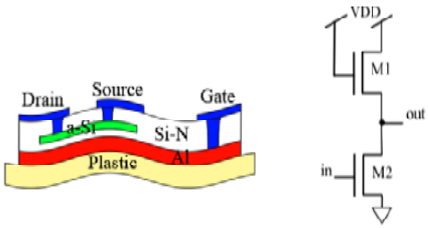

Fig. (1) Cross-section of flexible amorphous silicon thin film transistor (Left) and of amorphous silicon thin film transistor inverter (Right)

Since no PMOS or depletion mode NMOS transistors are available in a-Si technology, the load transistors are diode connected NMOS (Fig. 1). A drawback of this circuit configuration is reduced noise margin (Fig. 2). The eye opening in the curves is the static noise margin (SNM).

Generally, lower operating voltage has been beneficial to reducing integrated circuit power dissipation. However, the reduction in SNM of the a-Si inverter limits the lower operating voltage. The SNM of two coupled inverters are

depicted in Fig. (2) for typical process parameters. Operation at three different supply voltages of V_{DD}=30, 15 and 8V are shown. At 30V and 15V, the presence of the eye indicates that reliable storage is possible. However at 8V, the SNM vanishes and bi-stable operation cannot be maintained [8,9].

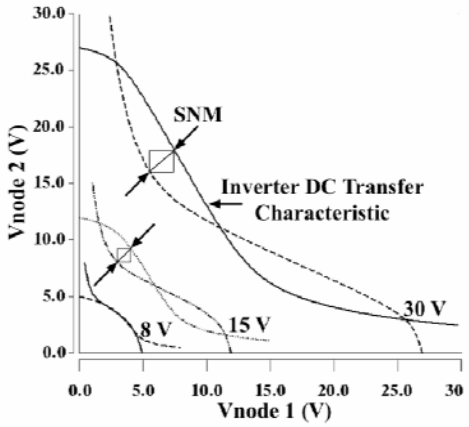

Fig. (2) Butterfly plot with V_t=3V, and V_{DD}=8V, 15V, 30V

The dynamic flip-flop in Fig. (3a) is the basis for the designs presented in this paper. The dynamic flip-flop is representative of digital machines in a-Si because it preserves state, has both static and dynamic current, and contains inverter structures common in combinational logic. The flip-flop is comprised of a master latch (transistors M1-M4) and a slave latch (transistors M5-M8) and uses two non-overlapping clocks, Φ_1, Φ_2. The master latch is clocked with Φ_1 followed by Φ_2. The last value of D at the end of Φ_1 is stored at node N2 at the rising edge of Φ_2. The slave latch is clocked with the same Φ_2 followed by Φ_1. The data at N2 is presented at Q at the rising edge of Φ_1. This operation is required to avoid a race-through condition [10]. The SPICE model parameters [11] correspond to the 9μm (effective gate length) technology at the Flexible Display Center [5]. For the simulation results presented in this paper, a 4-bit shift register is used, containing four flip-flops in series. The outputs are Q1-Q4. Additionally, the clock speed is bounded at the low end by the need to shift values through the chain before logic "1" values degrade due to leakage.

To optimize power reduction while preserving state, two cases are considered and described in the following sections. First, a word is dynamically stored in a recirculating shift register and the clock voltage is lowered. In the second case, we show both clocks being simultaneously driven to V_{DD} while feedback transistors provide static storage. This is then augmented with a low duty cycle clock to refresh the stored data. Analysis and simulation results are presented with each circuit, while section V concludes the paper.

3. Methods for Preserving State

A. Re-circulating Shift Register

The recirculation in the shift register is obtained with a feedback loop that is added to Q4 and feeds back to D. This enables a word to be dynamically stored. The simulation in Fig. (4) shows the data word with bit values "0101" shifting through the shift register with varying V_{DD} values of 30, 25, 20 and 15V and 25kHz clock, demonstrating correct operation at lower supply voltages.

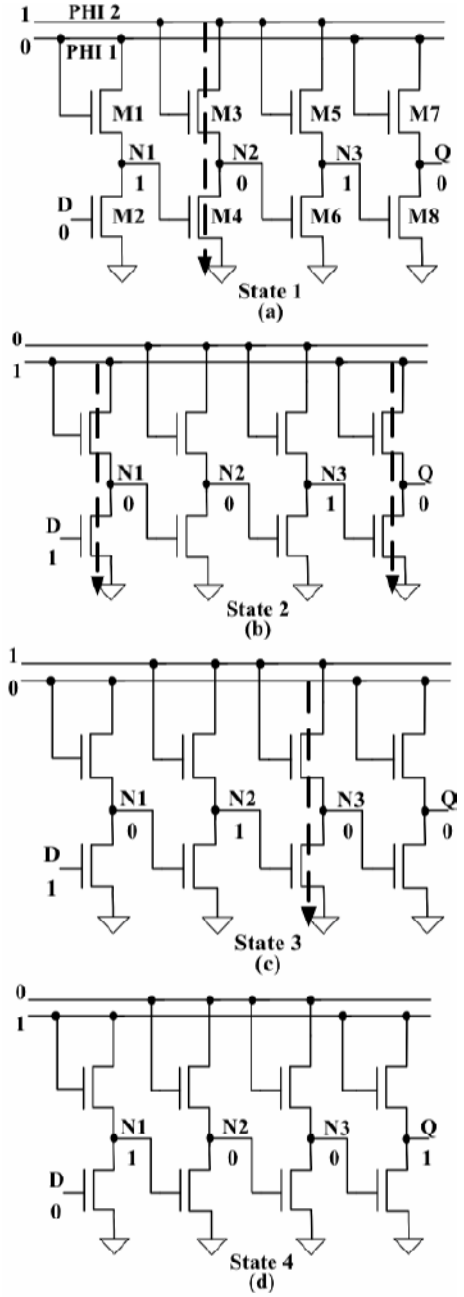

Fig. (3) Flip-flop standard cell showing four nodal states while loading a logic "1" after a logic "0". The dotted arrows indicate static current

The average power can be determined from the analysis of the flip-flop comprising Fig. (3). There will be static current when the input of an inverter is high and the corresponding clock (Φ_1 or Φ_2) is high. The dynamic current is active when the parasitic capacitance at a node (i.e. N1, N2, N3, and Q) is charging. These currents will be evident if the states of the nodes are known. Fig. (3) shows the standard flip-flop and the respective node values as a "1" is clocked into the circuit. On Φ_2 with D=0, there is one static current path in the flip-flop through node N2 and node N3 is dynamically charged (Fig. 3a). On the following Φ_2, with D=1, there are two static current paths (nodes N1 and Q) and no nodes dynamically charged (Fig. 3b). On the following Φ_1, there is one static current path (node N3) and node N2 is dynamically charged (Fig. 3c). Finally, on Φ_2, the output Q becomes 1. There are no static currents paths, and nodes N1 and Q are dynamically charged (Fig. 3d). A similar result is obtained for loading a '0' after a '1'. During recirculation, the flip-flop exhibits one static and one dynamic current on average. Therefore, the average power for an n-bit shift register is

$$P_{AVE} = n \cdot V_{DD} \cdot I_{DS} + n \cdot C \cdot V_{DD} (V_{DD} - V_t) \cdot f \qquad (1)$$

where n is the number of bits, I_{DS} is the static current, C is the parasitic capacitance of each node, f is the clock frequency, and V_t is the threshold voltage

Referring to the master latch in Fig. (3), the parasitic capacitances are calculated by grounding all the gates of M1-M3 and adding all the capacitances at each node, e.g. $C_{N1}=C_{gs1}+C_{gd2}+C_{gs4}+C_{gd4}$. For a 4-bit shift register with V_{DD}=30V, V_t=3V, and f=25kHz, the dynamic power is 138μW. With V_{DD}=15V, this is reduced to 31μW.

The static current can be calculated by equating the currents of the saturated load transistor and that of the pull-down transistor operating in the triode region. Using the conventional square law transistor I_{DS} equations the output voltage as a function of V_{DD} is

$$V_X(V_{DD}) = \frac{(V_{DD} - V_t) \cdot (\sqrt{S_{drive} + 2 \cdot S_{load}} - \sqrt{S_{drive}})}{\sqrt{S_{drive} + 2 \cdot S_{load}}} \qquad (2)$$

where S_{drive} and S_{load} are the width to length ratios of the drive and load transistor, respectively. When substituted back into the I_{DS} equation, Eq. (2) yields

$$I_{DS}(V_{DD}) = \mu \cdot C_{OX} \cdot S_{Load} (V_{DD} - V_X - V_t)^2 \qquad (3)$$

Substituting Eq. (3) into Eq. (1) gives the static power component. At V_{DD}=30V, the static power is 2712μW, and with V_{DD}=15V, this is reduced to 263μW. The total power as a function of V_{DD} is shown in Fig. (5). The static power is clearly dominant, unlike CMOS, because of the static paths and very low operating frequencies of a-Si circuitry. The recirculating shift register would require a frequency of 160MHz, well above current operating frequencies, for the dynamic power to equal the static power.

B. Static Feedback Shift Register with Refresh

An alternate approach to preserve state is to include static feedback in each latch. Static feedback loops and pass gates are added to the master and the slave latches in Fig. (6). Transistors M9 and M10 create the feedback loops and pass transistors M11 and M12 break the feed-forward paths. To enable recirculation, FBb is de-asserted low, turning M11 and M12 off and FB is asserted high, turning the feedback transistors M9 and M10 on. The circuit in Fig. (6) is now essentially an SRAM storage element. The SNM of the resulting element is the same as that shown in Fig. (2).

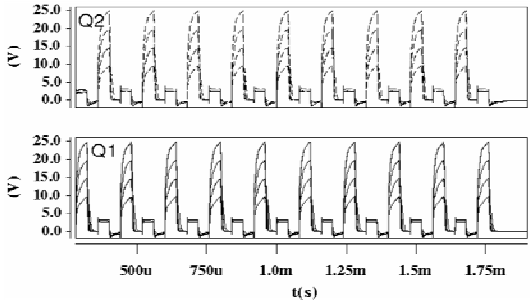

Fig. (4) Shifting a data word "0101" with V_t=3V and V_{DD} values of 30V, 25V, 20V, and 15V and frequency of 25kHz

The operation of the shift register holding state, where the clocks are simultaneously driven to V_{DD} (with V_{DD} values of 30, 25, 20, 15, and 10V), and shifting bits is shown in Fig. (7). The minimum value of the supply voltage is bounded by the collapse of the SNM below about 8V (Fig. 2). The hold state is evident at t=500μs when the clocks are asserted high and the feedback loops are activated. The clocks resume at t=1200μs and the circuit resumes operation at the point it left off. Nodes Q3 and Q4 show similar operation. While having one of the clocks at 0V at any moment in the previous case eliminated the static power component from inverters fed by that clock/supply, here this is not the case. Both of the clocks are on when statically holding state, meaning that static power is dissipated through nearly twice as many inverters as the previous case. Hence, the static power is nearly double when compared to the recirculating shift register (Fig. 5). Even though the dynamic power is eliminated and the static power is mitigated by reducing the supply voltage, this is still not sufficient. At V_{DD}=30V,

the power is 5118μW, and at 15V, power dissipation is reduced to 449μW.

Noting that static power can occur only in inverters when the associated clock/power supply is high suggests another approach. Using the same circuit (Fig. 6), but pulsing both clocks simultaneously to refresh the state allows both clocks to be low most of the time. This operation is depicted in Fig. (8). Here, high node voltages, i.e., those holding a "1" can be seen to decay due to leakage. Thus the clocks must be asserted often enough to refresh nodes before the voltage reaches 8V, the point at which the feedback inverter can no longer reliably identify the state of the input node (Fig. 2). The clocks need only be high long enough to refresh the high node values, limiting the duration of the static power dissipation, already shown to be the dominant term. By implementing a low duty cycle clock pulse, the total power dissipated in this scenario will be orders of magnitude lower. The dominating static power will only occur during the short time period when the clock is recharging the nodes, thus faster node charging means less static power dissipated. The large amount of time between clock pulses means the static power will be minimal, as is consistent with what has already been stated.

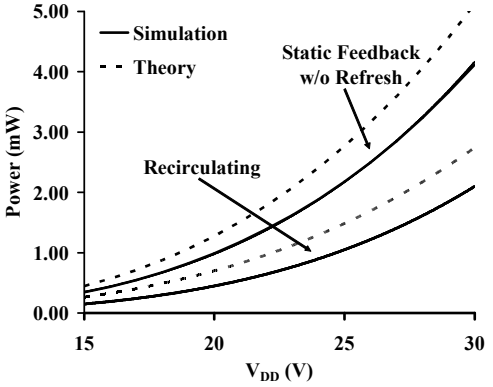

Fig. (5) The power of a 4-bit recirculating shift register and static feedback flip-flop. The average power is nearly double in the static feedback case without refresh

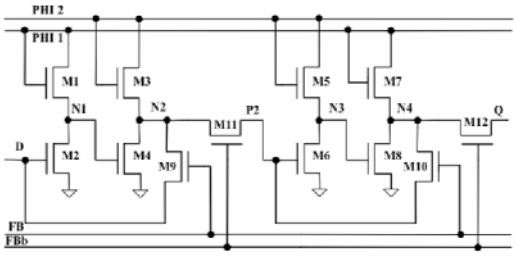

Fig. (6) Flip-flop design with pass and feedback transistors added

The lower bound on the low duty cycle clock frequency is determined by the transistor leakage I_{off}. I_{off} is calculated from the equations given in the model parameters of a-Si TFTs [11]. The refresh time is determined by the I_{on} current drive and the load at each node. I_{on} is a function of V_{DD} derived as I_{DS} in Eq. (3).

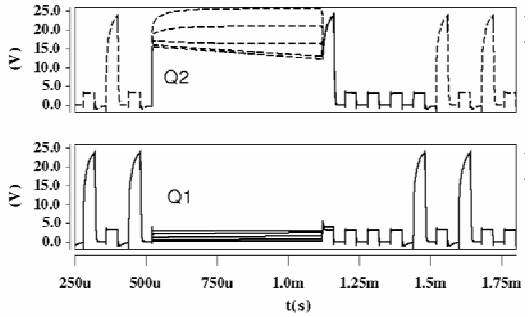

Fig. (7) Q1 and Q2 are holding a logic 0 and 1from 500μs to 1200μs, and then the shift register continues operation

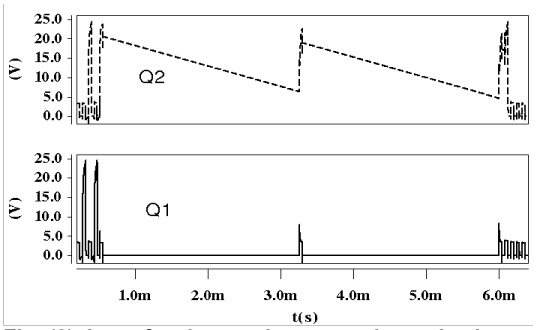

Fig. (8) Just after 3ms, voltages on the nodes have degraded to about 8V and are refreshed with the low duty cycle clock

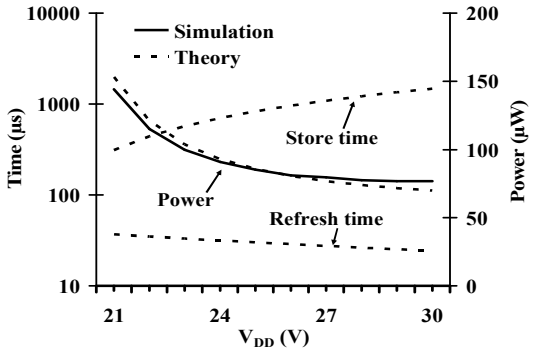

Fig. (9) Power consumption when using a low duty cycle clock to refresh nodes is about 75μW, about 36x less than the previous case. As V_{DD} is increased, it takes less time to charge nodes and the store time increases

The refresh time can be readily shown as

$$T_R = \frac{C}{k}[\ln(V_{meta} - V_{DD} + V_t) - \ln(V_f - V_{DD} + V_t)] \quad (4)$$

where C is the parasitic capacitance at a node (calculated earlier), V_f is 90% of the maximum output voltage, and V_{meta} is the metastable point, and $k=(W/L)\mu_o C_{ox}$. Fortunately, despite low current drive the a-Si TFTs have a high I_{on}/I_{off} ratio allowing long durations between refresh. This duration is given by

$$T_S = C \cdot \Delta V / I_{off} \quad (5)$$

where ΔV is the allowable voltage degradation (the difference between high voltage and V_{meta}.) Thus, the average power in this case is significantly reduced. The average power is readily shown as

$$P_{ave} = \frac{2 \cdot n \cdot I_{on} \cdot V_{DD} \cdot T_R + 2 \cdot n \cdot C \cdot V_{DD} \cdot (V_{out} - V_{meta})}{T_R + T_S} \quad (6)$$

Interestingly, the power consumption is lowest at high V_{DD} as evident in Fig. (9). At V_{DD}=21V, the power is 150μW, and at 30V, the power is reduced to 75μW. At high V_{DD}, while the dynamic power of each refresh operation is quadratically higher than at lower voltage, the retention time is maximized since there is greater stored charge and no substantial increase in I_{off} (the a-Si TFTs exhibit leakage current that does not depend strongly on drain voltage). A long retention time reduces the frequency and hence power consumption associated with the refresh cycles. This counter intuitive result is again explained by the dominance of static over dynamic power in a-Si TFT circuits.

4. Discussion

The recirculating shift register with reduced V_{DD} is a viable approach for reducing power while preserving state. At V_{DD}=30V, the power is 2712μW, and with V_{DD}=15V, the power is reduced to 263μW, a 10x power savings. However, there is a delay when reading data because the bits must recirculate to their proper positions. In addition, the power supply voltage needs to be dynamically lowered when the circuit is inactive and the state is preserved, requiring additional circuitry for that control.

An even better approach to reduce power while preserving state is to use the shift register with feedback and a low duty cycle clock. At V_{DD}=21V, the power is 150μW, and at 30V, the power is reduced to only 75μW. The lower average power at the higher voltage is a result of the longer time between refresh pulses. The disadvantage is the additional transistors for feedback. Using the shift register with feedback at a V_{DD} of 30V, there is a 36x power savings compared to the recirculating shift register at the same V_{DD} and a 3x power savings relative to the recirculating shift register with a reduced V_{DD} of 15V. Consequently, the shift register with feedback and a low duty cycle clock is the most promising approach to reduce power in digital a-Si circuits while preserving state.

5. Conclusion

Lacking a p-type transistor, problems for reducing power are reintroduced from the 1970's. Also, the low mobility of a-Si TFTs require high rail voltages further increasing static power consumption. Because these circuits operate at low frequencies, high supply voltages, and have diode connected load transistors, dynamic power is small in comparison to static power. Thus the design focus is on reducing static power. Using the static flip-flop with feedback and a refresh based operating mode, the total power of the circuit while in hold state is significantly reduced. At V_{DD}=30V, the power has been reduced by 36x compared to retention via conventional recirculating shift registers.

References

[1] T. Tsukada, **"Active matrix liquid crystal displays",** in Technology and Applications of Hydrogenated Amorphous Silicon, R.A. Street, Ed., Springer (NY) (2000) 7-93.
[2] K.S. Karim et al., *IEE Proc. Circuits Devices Syst.*, 150(4) (2003) 267-273.
[3] M. McCreary, "Recent Advances in Electrophoretic Displays on the Road to Electronic Paper," in Proc. of the Flexible Displays and Microelectron. Conf., Phoenix, Arizona, February 10-12, 2004.
[4] M. Hack et al., "Flexible Low Power Consumption AMOLED Displays", in Proc. of the Flexible Displays and Microelectron. Conf., Phoenix, Arizona, February 1-3, 2005.
[5] The Flexible Display Center (FDC) at Arizona State University (flexdisplay.asu.edu).
[6] K.S. Karim et al., *IEEE Electron Device Lett.*, 25(4) (2004) 188-190.
[7] Available from the Sarnoff Corp., www.sarnoff.com/products.
[8] Bruce Bateman, "High-speed SRAM Design", ISSCC Tutorial (1998).
[9] E. Seevinck, F.J. List and J. Lohstroh, *IEEE JSSC*, SC-22(5) (1987).
[10] W. Lu, "Flat Panel Display Drive Circuits", M.Sc. thesis, Dept. Electr. Eng., Arizona State Univ., Tempe, AZ, (May 1990).
[11] M.S. Shur et al., *J. Electrochem. Soc.*, 144(8) (1997) 2833-2839.

SPIE *Society of Photonics Instrumentation Engineers*

FORTHCOMING CONFERENCES

International Photodynamic Association World Congress 2009
Date(s): 11 - 15 June 2009
Location: Seattle, Washington, USA

European Conferences on Biomedical Optics
Date(s): 14 - 18 June 2009
Location: Munich, Germany

Mirror Technology SBIR/STTR Workshop
Date(s): 16 - 18 June 2009
Location: Albuquerque, New Mexico, USA

ISPDI 2009 - International Symposium on Photoelectronic Detection and Imaging
Date(s): 17 - 19 June 2009
Location: Beijing, China

Education and Training in Optics and Photonics 2009
Date(s): 5 - 7 July 2009
Location: St. Asaph, North Wales, United Kingdom

SPIE Optics + Photonics
Date(s): 2 - 6 August 2009
Location: San Diego, California, USA
Exhibition Date(s): 4 - 6 August 2009

SPIE NanoScience + Engineering
Date(s): 2 - 6 August 2009
Location: San Diego, California, USA

SPIE Solar Energy + Technology
Date(s): 2 - 6 August 2009
Location: San Diego, California, USA

SPIE Photonic Devices + Applications
Date(s): 2 - 6 August 2009
Location: San Diego, California, USA

SPIE Optical Engineering + Applications
Date(s): 2 - 6 August 2009
Location: San Diego, California, USA

SPIE Europe Remote Sensing
Date(s): 31 August - 3 September 2009
Location: Berlin, Germany
Exhibition Date(s): 1 - 2 September 2009

SPIE Photomask Technology
Date(s): 14 - 17 September 2009
Location: Monterey, California, USA
Exhibition Date(s): 15 - 16 September 2009

Laser Damage Symposium on Optical Materials for High Power Lasers
Date(s): 21 - 23 September 2009
Location: Boulder, Colorado, United States

Inter-Institute Workshop on Optical Diagnostic and Biophotonic Methods from Bench to Bedside
Date(s): 1 - 2 October 2009
Location: Bethesda, Maryland, USA

20th International Conference on Optical Fibre Sensors
Date(s): 5 - 9 October 2009
Location: Edinburgh, United Kingdom

International Conference on Optical Instrumentation and Technology
Date(s): 19 - 22 October 2009
Location: Shanghai, China

International Symposium on Multispectral Image Processing and Pattern Recognition
Date(s): 30 October - 1 November 2009
Location: Yichang, China

ACP 2009 - Asia Communications and Photonics Conference and Exhibition
Date(s): 2 - 6 November 2009
Location: Shanghai, China
Exhibition Date(s): 4 - 6 November 2009

SPIE Lithography Asia - Taiwan
Date(s): 18 - 20 November 2009
Location: Taipei, Taiwan
Exhibition Date(s): 18 - 19 November 2009

Range-Coverage Extension Using Smart Antennas in Mobile Communications Systems

Adheed H. Sallomi [1]
Sana R. Salim [2]

[1]*Department of Electrical Engineering, College of Engineering, Al-Mustansiriyah University, Baghdad, Iraq*
adalameed@yahoo.com
[2]*Department of Physics, College of Sciences, Al-Mustansiriyah University, Baghdad, Iraq*

The growing demand for wireless communications services is constantly increasing the need for better coverage and quality service. Smart antennas employ collection of individual elements in the form of an array, so, they give rise to narrow beam with increased gain when compared to conventional antennas using the same power. The array gain is the average increase in signal power at the receiver due to a combination of the signals received at all antenna elements. The gain provided by adaptive antenna array is proved to provide an extension in a communication range that depends on the number of array elements. The simulation had done by using power exponent radio wave propagation model shows that the gain provided by smart antennas can extend the range of a cell to cover a larger area and more users than would be possible with omnidirectional or sector antennas. The increase in gain leads to employ fewer base stations to cover a given area.

Keywords: Wireless technology, Radioactive waves, Smart antenna
Received: 23 December 2008, **Revised**: 20 April 2009, **Accepted**: 2 May 2009

1. Introduction

The wireless (cellular) technology is partially replacing the use of the wired telephone network. Cellular systems accommodate a large number of mobile units over a large area within a limited frequency spectrum.

A cellular network consists of a large number of wireless subscribers who have cellular telephones (users) that can be used in cars, in buildings, or almost anywhere. There are also a number of fixed base stations, arranged to provide coverage of the subscribers [1]. The unit area of RF coverage for cellular is called a cell. In each cell, a base station transmits from a fixed cell site location, which is often centrally located in the cell, to mobile stations. Base stations are supported by, and interconnected to each other and the public switched telephone network (PSTN) via mobile switching center (MSC), as illustrated in Fig. (1) [2-3].

The coverage area is simply the area in which communication between a mobile and the base station is possible. Range extension is a means of increasing coverage area [1]. The channels used for transmission from the base station to the mobiles are called forward or downlink channels, and the channels used for transmission from the mobiles to the base station are called reverse or uplink channels [4].

2. Smart Antenna Systems

Each base station has towers that support several transmitting and receiving antennas. Omni-directional or sectored antennas used in base stations of mobile communication systems, can be considered as an inefficient use of power as most of it has been radiated in other directions than toward the user as shown in Fig. (2) [1]. Besides, other users can experience interference from this "stray" radiated power [5].

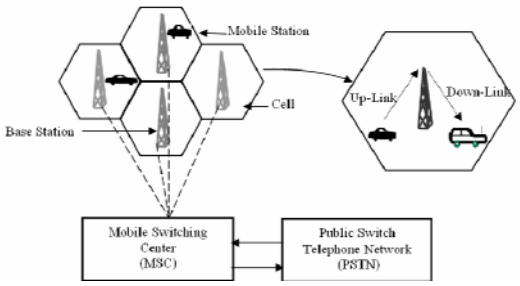

Fig. (1) Basic cellular communication system 2-smart antenna systems

The idea of smart antennas is to direct a single beam to each user to optimize the radio performance and to increase the communication system range as shown in Fig. (2). Smart antennas consist of an array of antenna elements and a smart processing of antenna signals. The goal of smart antenna is to receive in the uplink as much power as possible from the desired

mobile station. In the downlink as much power as possible has to be transmitted into the direction of the desired mobile station [6-7] .

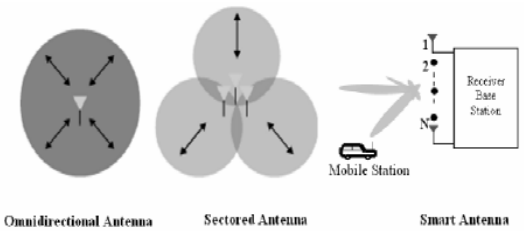

Fig. (2) Base station antennas [3]

During using smart (adaptive) antenna array of M elements the signal amplitude increases (M) times because the desired signal received at each antenna element is phase-shifted due to weight coefficient, and then the signal components from each element are positively combined [8-9].

The gain provided by smart antennas can extend the range of a cell to cover a larger area and more users than would be possible with omnidirectional or sector antennas [11]. The interference-rejection capability of the smart antenna system provides significanlly more coverage than either omnidirectional, or sectorised antennas as it can direct its beam in the direction of the user of interest [12].

3. Power Exponent Radio Wave Propagation Model

In planning cell coverage area the goal is to estimate the electric field strength of the transmitted signal at the receiver end (perimeter of coverage area) [11].

Friis transmission equation relates the power received to the power transmitted between two antennas separated by distance large enough for each antenna to be in the far field region of the other. This equation is given as,

$$\frac{P_r}{P_t} = \left(\frac{\lambda}{4\pi d}\right)^2 . G_t G_r \qquad (1)$$

The power exponent model is also used to predict the power transfer between a transmitter and a receiver in different environments. The received power (P_r) at distance (d) from the transmitting antenna can be expressed with respect to the power measured at a certain standard distance (d_o), i.e. the reference power ($P_r(d_o)$) [8].

$$P_r(d) = P_r(d_o).\left(\frac{d_o}{d}\right)^{\gamma} \quad for \quad d > d_o \qquad (2)$$

where (d_o) is a reference distance, that is chosen to be in the far-field of the antenna, and considered to be close enough to the transmitter such that multipath and diffraction are negligible. This model takes into account the decrease in energy density suffered by the radio wave due to spreading, as well as the energy loss due to the interaction of the wave with the propagation environment. The signal loss (L_P) at distance (d) from the transmitting antenna can be expressed as:

$$L_p(d) = L_p(d_o).\left(\frac{d_1}{d_o}\right)^{\gamma} \quad for \quad d > d_o \qquad (3)$$

The value of (γ) depends on specific features of the propagation environment and it is between (2) and (5). Larger values of (γ) correspond to more obstruction and hence faster decrease in average received power as distance become larger [1].

4. Coverage Extension during Using Smart Antennas

We used the power exponent model to derive the approximate relationship of coverage area to antenna gain (G).

The array gain (G) is the average increase in signal power at the receiver due to combination of the signals received at all antenna elements. It is proportional to the number of antennas. For an array of M antenna elements, the resultant beam gain is:

$$(Array\ Gain)_{dB} = G = 10\log_{10} M \qquad (4)$$

If for a single antenna the highest permissible attenuation level (path losses) is achieved at the distance (d_1) from the base station, then after application of smart (adaptive) antenna array the same attenuation is achieved at the distance (d_2), where

$$L_p(d_2) = L_p(d_1) + G \qquad (5)$$

$$L_p(d_o) + 10\log\left(\frac{d_2}{d_o}\right)^{\gamma}$$

$$= L_p(d_o) + 10\log\left(\frac{d_1}{d_o}\right)^{\gamma} + G \qquad (6)$$

$$G = 10\log\left(\frac{d_2}{d_o}\right)^{\gamma} - 10\log\left(\frac{d_1}{d_o}\right)^{\gamma} \qquad (7)$$

$$G = 10\log\left(\frac{d_2}{d_o}.\frac{d_o}{d_1}\right)^{\gamma} = \log\left(\frac{d_2}{d_1}\right)^{10\gamma} \qquad (8)$$

From the logarithm definition and assuming that the value of (γ) is equal to (4) for urban environment, we can write:

$$10^{G} = \left(\frac{d_2}{d_1}\right)^{40} \qquad (9)$$

$$10^{\frac{G}{40}} = \left(\frac{d_2}{d_1}\right) = Range\ Extension\ Factor = \rho \qquad (10)$$

$$\log\rho = 0.25\log M = \log M^{0.25} \qquad (11)$$

The additional gain results in extending the range (area) of the cell.

$$\rho = \frac{d_2}{d_1} = M^{0.25} \qquad (12)$$

$$\because A_2 = A_{smart} = \pi.(d_2)^2$$
$$and\ .A_1 = A_{omni} = \pi.(d_1)^2 \quad (13)$$

$$\left(\frac{A_2}{A_1}\right) = \left(\frac{d_2}{d_1}\right)^2 = \left(M^{0.25}\right)^2 \quad (14)$$

$$\left(\frac{A_2}{A_1}\right) = M^{0.5} = \sqrt{M} \quad (15)$$

Range extension is suited to rural areas, where the user density is low and it is desirable to cover as much area with as few base stations as possible [11].

5. Base Station Reduction

The additional coverage of a base station means that an operator can achieve a substantial reduction in infrastructure costs, due to the reduction in required base stations.

Assuming that the base stations are distributed uniformly in a considered area (A), then to increase the cell radius from (d_1) (the area of a single cell is (A_1) to (d_2) (the cell area is now (A_2), the necessary base stations decrease according to the reduction factor (g) which is given by:

$$g = \frac{A/A_2}{A/A_1} = \frac{A_1}{A_2} = \frac{\pi.(d_1)^2}{\pi.(d_2)^2} = \frac{(d_1)^2}{(d_2)^2} = \left(\frac{1}{\rho}\right)^2 \quad (16)$$

$$\rho = M^{0.25} \quad (17)$$

$$g = M^{-0.5} \quad (18)$$

Fig. (3), shows the range-coverage extension factor against the number of smart antenna elements. Fig. (4), shows the base stations reduction factor against the number of smart antenna elements. It can be seen that using eight elements smart antenna can reduce the number of base station by a factor of 35%.

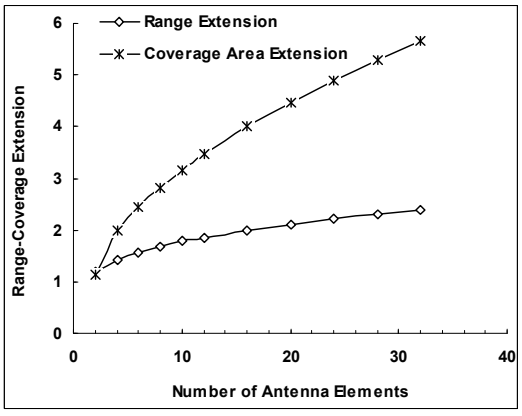

Fig. (3) Number of array elements and range-coverage extension

6. Simulation of Coverage Extension by Smart Antennas

The power exponent model has been used to simulate the benefits achieved during using smart antenna of eight elements (M=8), in a base station of a mobile communication system. For this simulation, the reference distance (d_o) is set to be 720m and the transmitted power is set to be 0.6 watt (27.78dBm) in up-link.

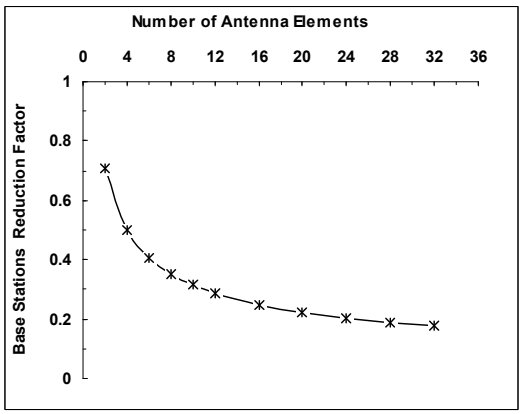

Fig. (4) Number of array elements and base station reduction factor

Fig. (5), shows that when a subscriber unit transmits 0.6W (27.78dBm), the power received at a base station located 2km away from the mobile unit will receive (-78.638dBm), during using omnidirectional antenna, while it will equal to (-69.608dBm), when array of eight elements used at the base station. The difference is due to the gain obtained by using the array (10log(8)). The gain obtained in smart antenna allows base station to transmit lower power, resulting in overall electrical power cost saving.

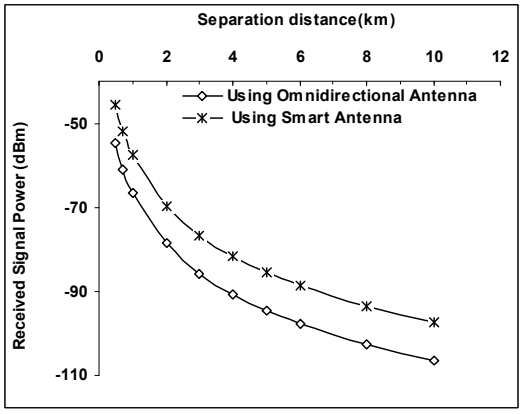

Fig. (5) The received signal power using omnidirectional and smart antenna

The plot of maximum separation distance (range) against the transmitted power is shown in Fig. (6). It can be noticed that when the transmitted power is 1W the maximum separation distance is 5.5km during using omnidirectional antenna while it is 9.25km when a smart antenna of eight elements is used. The maximum separation distance increases by a factor of 68% during using smart antenna. This means that base stations can be placed

further apart leading to a more cost-efficient development.

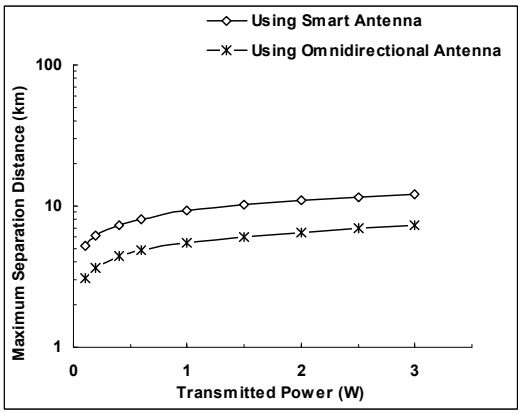

Fig. (6) The maximum separation distance in urban environments using omnidirectional and smart antenna

7. Conclusion

The smart antenna gain compared to a single element antenna can be increased by an amount equal to the number of array elements. Because smart antennas is more directive than sector or omnidirectional antennas, it can provid an additional gain , so it can extend the range of a cell to cover an area that is larger by $(\sqrt{M})$ than would be possible with omnidirectional or sector antennas.

Using smart antenna arrays reduces the number of base station required for a mobile system by amount of $(1/\sqrt{M})$. Using antenna arrays with M elements, for mobile communication systems will help in producing better quality beam patterns in terms of directivity and coverage.

References

[1] A.H. Sallomi, "Smart Antenna Performance Analysis for Mobile Communications in Urban Environments", Ph.D. thesis, University of Technology, Baghdad, (2007).

[2] P. Cardieri and T.S. Rappaport, *IEEE Trans. on Vehicular Technol.*, 50(2) (2001), 1-11.

[3] V. Selvarju, "Normalised Least Mean Squared algorithm for Smart Antenna Systems", Ph.D. thesis, University of Queensland, Australia (2003) 9-24.

[4] W. Krzysztof, **"Mobile Communication Systems"**, John-Willy & Sons Ltd, 1st ed. (2002) 427-439.

[5] L.G. Godara, *Proc. of IEEE*, 85(8) (1997) 1195-1247.

[6] Sadiku, N.O. Matthew, **"Elements of Electromagnetic"**, 3rd ed., Oxford University Press (2002), ch. 18, 612-621.

[7] S.S. Foo, "Smart Antennas for Wireless Applications, Undergraduate thesis, Department of Computer Sciences and Electrical Engineering, University of Queensland, Brisbane, Australia (2000) 35-37.

[8] Rappaport, S. Theodore and K. Blankship, "Propagation and Radio System Design Issues in Mobile Radio Systems", Virginia Polytechnic Institute (1997) 3-10.

[9] F.T. Ulaby, "Fundamentals of Applied Electromagnetic", Prentice Hall, New Jersey, (1997).

[10] A. El-Zooghby, *IEEE Antennas and Propagation Mag.*, 43(5) (2001) 172-177.

[11] F. Rayal, *IEEE Antennas and Propagation Mag.*, 47(6) (2005) 124-127.

[12] S. Bellofiore, C. Balanis and J. Foutz, *IEEE Antennas and Propagation Mag.*, 44(3) (2002) 145-154.

Fawwaz J. Jibrael*
Hussain A. Hammas

Department of Electrical and Electronic Engineering, University of Technology, Baghdad, Iraq
** fawaz_eng2007@yahoo.com*

Analysis and Design of Combined Fractal Dipole Wire Antenna

This paper presents the analysis and design of a small size, low profile and multiband combined fractal Koch dipole antenna. The proposed antenna design, analysis and characterization have been performed using the method of moments (MoM) technique. The new designed antenna has operating frequencies of 440MHz, 1194MHz, and 5272MHz with acceptable bandwidth, which has useful applications in communication systems. The radiation characteristics, VSWR, reflection coefficient, and input impedance of the proposed antenna are described and simulated using 4NEC2 software package. Also, the gain of this proposed antenna is calculated and described in the three planes: XZ-plane, YZ-plane, and XY-plane, where the antenna is placed in the YZ-plane.

Keywords: Koch curve, Fractal antenna, Dipole antenna, Multiband antenna
Received: 22 April 2009, **Revised**: 5 May 2009, **Accepted**: 12 May 2009

1. Introduction

A wide variety of applications of fractals can be found in many branches of science and engineering. One such area is fractal electrodynamics. Fractal geometry can be combined with the electromagnetic theory for the purpose of investigating a new class of radiation, propagation and scattering problems.

One of the most promising areas of fractal electrodynamics research is in its application to antenna theory and design. There are a variety of approaches that have been developed over the years, which can be utilized to achieve one or more of these design objectives pertaining to size, gain, efficiency and bandwidth. Unique properties of fractals can be exploited to develop a new class of antenna element designs that are multi-band, compact in size and can possess several highly desirable properties, including multi-band performance, low side lobe levels, and their ability to develop rapid beam forming algorithms based on the recursive nature of fractals [1].

Fractal shapes radiate signals at multiple frequency bands, occupy space more efficiently and offer design solutions meeting the requirements for antennas in future wireless devices such as cell phones and other wireless mobile devices such as laptops on wireless local area networks (LAN).

Fractal was first defined by Benoit Mandelbrot [2] in 1975 as a way of classifying structures whose dimensions are not whole numbers. These geometries have been used previously to characterize unique occurrences in nature that were difficult to define with Euclidean geometries, including the length of coastlines, the density of clouds, and branching of trees. Fractal antennas have been demonstrated to enhance antenna properties due to their self-similarity behavior. Multiband behavior for Koch monopole and dipole is demonstrated in [3].

2. Proposed Antenna Geometry

The triangle Koch curve and quadratic Koch curve geometries [4], with different iterations are shown in Fig. (1).

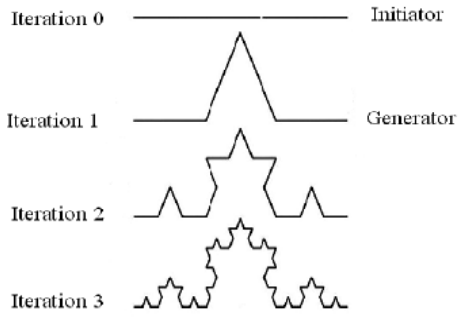

(a) Triangle Koch curve

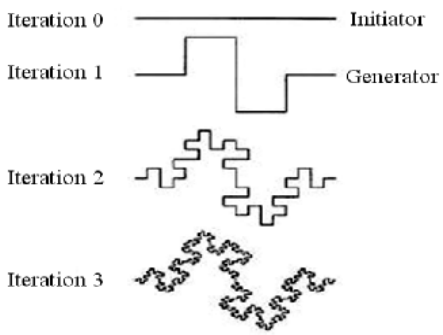

(b) Quadratic Koch curve

Fig. (1) First three iterations of the construction of the triangle and quadratic Koch curve

The proposed antenna geometry is combined from first iteration of triangle and quadratic Koch curve geometries, where one of the fractal geometries replaced with the segment lines of the other fractal geometry. The proposed antenna geometry is shown in Fig. (2).

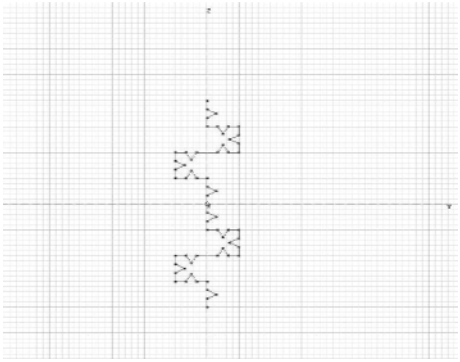

Fig. (2) Combined Koch curve dipole antenna

Fractal dimension contains used information about the self-similarity and the space-filling properties of any fractal structures [2]. The fractal similarity dimension (*FD*) of the proposed antenna is defined as:

$$FD = \frac{\log(N)}{\log(1/\varepsilon)} = \frac{\log(32)}{\log(12)} = 1.39$$

where N is the total number of distinct copies, and $(1/\varepsilon)$ is the reduction factor value which means how will be the length of the new side with respect to the original side length.

3. Proposed Antenna Design

The dipole antenna based on the combined fractal Koch antenna has been modeled, analyzed, and its performance has been evaluated using the commercially available software 4NEC2. The method of moment (MoM) is used to calculate the current distribution along the combined Koch dipole antenna and hence the radiation characteristics of the antenna [5]. The layout of this antenna with respect to the coordinate system is shown in Fig. (2). The modeling process is simply done by dividing all straight wires into short segments where the current in one segment is considered constant along the length of the short segment. It is important to make each wire segment as short as possible without violation of maximum segment length to radius ratio computational restrictions. In NEC, to modeling a wire structures, the segments should follows the paths of conductor as closely as possible [6].

The feed source point of this antenna is placed at origin (0, 0, 0), and this source set at 1 volt. The design frequency has been chosen to be 750MHz for which the design wavelength λ is 0.4m (40cm) then the length of the corresponding λ/2 dipole antenna length will be of 20 cm, as shown in Fig. (2). Figure (3) shows the visualization of this dipole antenna geometry by using NEC-viewer software.

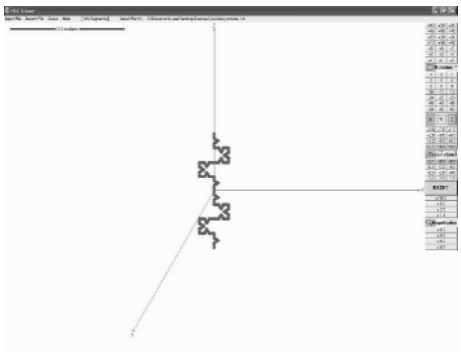

Fig. (3) Visualization of the modeled dipole antenna geometry

4. Antenna Simulation Results

In this work, Method of Moment simulation code (NEC) is used to perform a detailed study of VSWR, reflection coefficient, gain, input impedance and radiation pattern characteristics of the combined Koch dipole antenna in a free space.

The real and imaginary parts of the input impedance of this proposed antenna are shown in Fig. (4) over a frequency range from 0 to 6GHz. The input impedance characteristics of this proposed antenna show the multiple resonance characteristics of the antenna.

VSWR of the antenna is shown in Fig. (5). It is found that the antenna has triple bands behavior at the resonance frequencies 440MHz, 1194MHz, and 5272MHz with acceptable bandwidth.

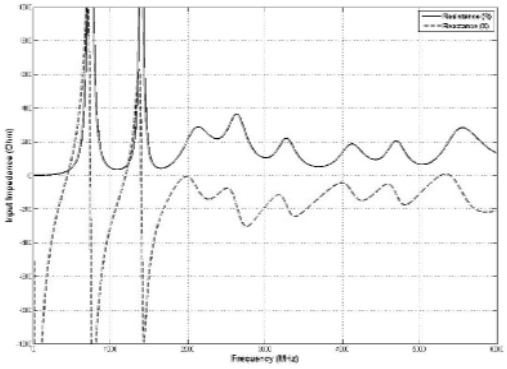

Fig. (4) Antenna input impedance

Table (1) shows these resonant frequencies and the corresponding input impedance of each one, with VSWR and reflection coefficients, while table (2) shows the gain of each frequency in the three planes XZ-plane, YZ-plane, and XY-plane, where the antenna is placed in the YZ-plane. The radiation patterns at these resonant frequencies in the planes YZ-plane, XZ-plane,

and XY-plane are depicted in Fig. (6), where the antenna is placed in the YZ-plane.

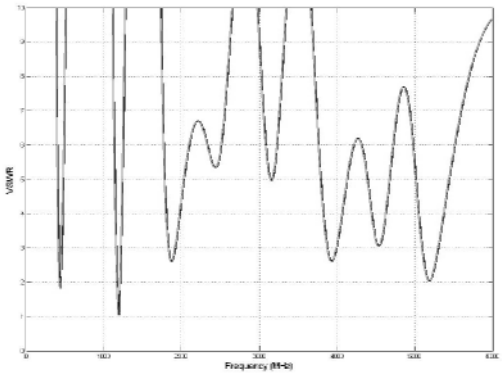

Fig. (5) Simulated 50Ω, VSWR vs. Frequency

Table (1) Resonant Frequencies and Input Impedances for Proposed Antenna

Frequency (MHz)	Input impedance (Ω)		VSWR	Reflection coefficient (dB)
	R	X		
440	27.21	j0.61	1.838	-10.6
1194	52.85	j0.394	1.058	-31.1
5272	129.5	j0.101	2.59	-7.07

Table (2) The Gain of the Proposed Antenna at the Resonant Frequencies in the Three Planes

F(MHz)	Gain (dB)		
	XY-plane	XZ-plane	YZ-plane
440	1.98	1.98	1.87
1194	0.74	1.65	4.27
5272	1.23	4.06	3.25

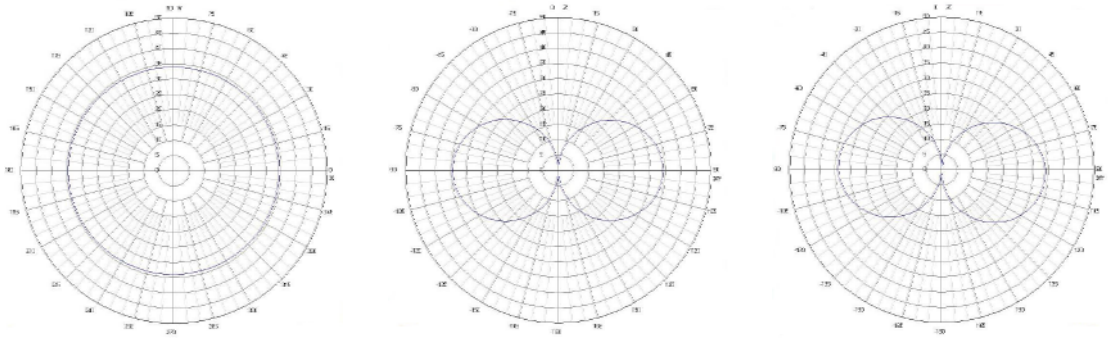

XY-plane **XZ-plane** **YZ-plane**

(a) f= 440 MHz

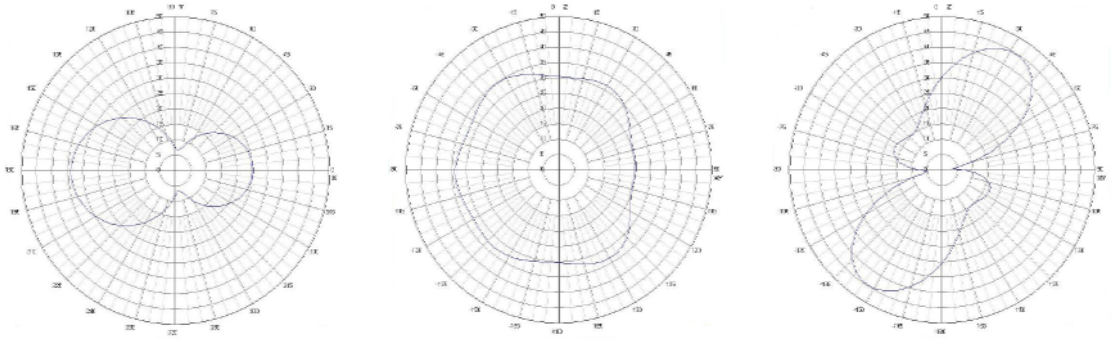

XY-plane **XZ-plane** **YZ-plane**

(b) f= 1194 MHz

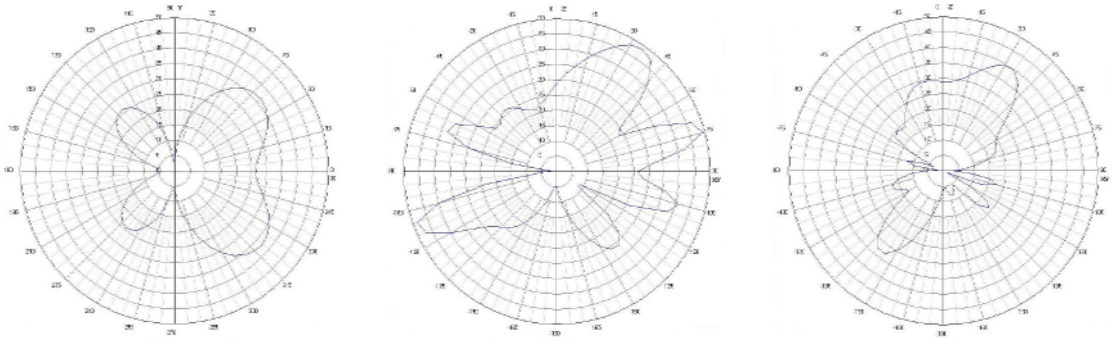

XY-plane **XZ-plane** **YZ-plane**

(c) f= 5272 MHz

Fig. (6) Radiation Patterns of the Modeled Antenna at Resonant Frequencies of (a) *f*=440MHz, (b) *f*=1194MHz, (c) *f*=5272MHz

5. Conclusions

In this work, the combined fractal Koch curve dipole antenna is investigated and its performance is evaluated. The simulation results show that this antenna can be efficiently operated as a multiband antenna and is compact in size. The proposed antenna has three resonance bands at frequencies of 440 MHz, 1194 MHz, and 5272 MHz. According to these frequencies, this antenna can operate as a multiband antenna in the UHF/SHF applications. Once optimized for radiation characteristics, this antenna can find many applications in UHF/SHF communication systems. It is expected that the proposed antenna can find extensive applications in the modern comp at wireless system after suitable frequency scaling and proper feeding.

References

[1] M. Sindoy, G. Ablat and C. Sourdois, C., *Electron. Lett.*, 35 (1999) 181-182.

[2] Falconer, K., "**Fractal Geometry: Mathematical Foundation and Applications**", John-Wiley & Sons, England (1990) 233.

[3] S.H. Zainud-Deen et al., "Radiation and Scattering from Koch Fractal Antennas", *21st National Radio Science Conf. (NRSC)*, March (2004) B8, 1-9.

[4] P.S. Addison, "**Fractals and Chaos: An Illustrated Course**", Institute of Physics Publishing Bristol and Philadelphia (1997) 98.

[5] C.A. Balanis, "**Antenna Theory: Analysis and Design**", 3rd ed., John-Wiley & Sons (2005) 115.

[6] G.J. Burke and A.J. Poggio, "**Numerical Electromagnetic Code (NEC)-Program description**", Lawrence Livermore Laboratory, January (1981).

Abdulmahdi Taleb [1]
Kais A. Al-Naimee [1,2*]
Soudad S. Ahmed [1]
Riccardo Meucci [2]

[1] *Department of Physics, College of Science, University of Baghdad, Baghdad, Iraq*
[2] *Istituto Nazionale di ottica Applicata,Florence, Italy*
[*] *kais.al-naimee@inoa.it*

Efficiency Enhancement of Photovoltaic Silicon Cell by Ultrashort Laser Pulses

We present an experimental evidence of the effect of the femtosecond laser pulses on the spectral response of the Silicon photovoltaic cell. The response of this device is covering the visible to near infrared spectral region. The responsivity of the photovoltaic solar cell is enhanced from 0.18A/W to 0.25A/W and/or the conversion efficiency increase from about 9% to about 14% due to irradiation effect. All treatments and measurements are made at room temperature. Results show that the responsivity is enhanced and the nano-structured groves of the 700-900 nm range are observed.

Keywords: Efficiency, Ultrashort pulses, Photovoltaics, Nanostructure
Received: 9 March 2009, **Revised**: 15 April 2009, **Accepted**: 22 April 2009

1. Introduction

Silicon is the most commonly used semiconductor in optoelectronic devices and silicon photodiodes are often used in industrial applications are reliable devices for light to electricity conversion. High operations Silicon photodiodes are preformed between their spectral responsivity. These features are especially important in the field of optical radiometry in which measurements of photometric and radiometric quantities have to be done with a high level accuracy.

The description of high accuracy interpolation of quantum yield of Silicon photodiode detectors in the near UV is presented by Kübarsepp et al [1]. The results of the of the quantum yield calculations and of measurements obtained by use of a Silicon trap detector are presented and compared. Since the year 1969 the amorphous Silicon plays a crucial role in producing lower cost-effective solar cells. However, the solar cells made from this material tend to have lower energy conversion efficiency than bulk silicon.

Carey et al [2] investigated the I-V characteristics and responsivity of photodiodes fabricated with silicon that was micro structured by use of femtosecond laser pulses in a Sulfur-containing atmosphere [2]. The Silicon surfaces irradiated with high intensity nanosecond laser pulses in the presence of Sulfur-containing gases have near unity absorption from near UV (250nm) to NIR (2500nm) at photon energies well below the bandgap of ordinary Silicon [3].

Microstructures developed spontaneously on Silicon surface under the cumulative short laser pulses irradiated in different ambient atmosphere [4,5]. The experimental results reveal that the ambient atmosphere and the laser pulse duration play key roles on the microstructures formation. In the present work, the experimental procedure to enhance the efficiency of a bare silicon solar cell from 9% to 14% is explained and the enhancement through out demonstrating the effect of femtosecond laser irradiation on Silicon surface is presented.

2. Experimental Procedure

As standard mechanism of spectral measurements (Fig. 1), the spectral response of the samples is measured after and before the irradiation process using femtosecond laser source and a calibrated detection unit. The system instrumentation is controlled from a PC via RS232 interface. The output of the monochromator is directed to two output windows, to the calibrated detector and the other to the sample under test. During the system operation a broad band light source is passed through a monochromator signaling out the desired frequency of the light to illuminate the photodiode.

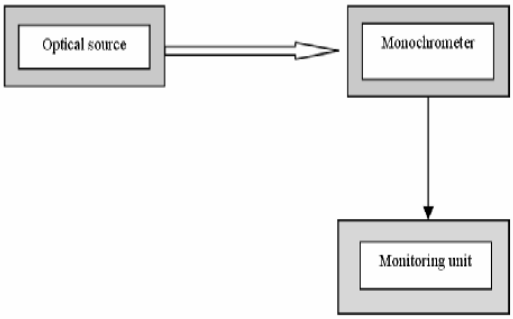

Fig. (1) The spectral measurement setup

The intensity of the light is measured with a calibrated detector and stored on the PC. The

photovoltaic devices current is measured with the semiconductor parameter analyzer and the results are stored on the PC. The measurement is then repeated over a range of wavelength between 400-900nm.

The sample understudy was irradiated by a tunable mode-locked Ti:sapphire oscillator laser source with 100fs pulse duration, 80MHz frequency at 800nm wavelength of operation. The sample was irradiated by this laser and a focusing objective with high numerical aperture was used in air environment. The laser beam was expanded by a 1x4 beam expander and it was focused on the target by means of 100mm focal length lens. The irradiating beam was directed normal to the anode side of the sample. The irradiation processes created numerous defect sites and modified the sample surface.

The behavior is identical at different wavelengths, 532nm and 810nm. The time response of the irradiated and unirradiated samples to nanosecond laser pulses has been taken into account. The output of the sample is connected by 50Ω to an oscilloscope for collecting data. Scanning Electron Microscope (SEM) images of the structures obtained in air environment. One line scan was performed at a fixed scan speed. A periodic structure (lines) was formed and observed in the range of 700-900nm range. The SEM images shows a semi periodic structure known as ripples or grooves in submicrostructure and were found after laser irradiation, Fig. (2).

As a conclusion, we believe that the use of this approach leads to enhance the spectral response of photovoltaic cell. The low intensities defining the laser irradiation drastically change the scale of the surface reshaping process, promoting the formation of nanostructures and the interaction between surface roughness and/or smoothness lead to increase the number of pulses contributing certainly to rapid nano-channels formation with very small spacing.

This approach leads to a new generation of photovoltaic solar cells and could be used to enhance a photovoltaic material responsivity and hence the conversion efficiency. Although the efficiency of the amorphous Silicon based solar cells were increased from 7% to about 9% during the last 40 years utilizing different methods, the stepping to 14% efficiency is considered as a big step by only rearranging the micro crystal structure of the cell surface utilizing ultrashort laser pulses which should be still economically reasonable in a large scale production.

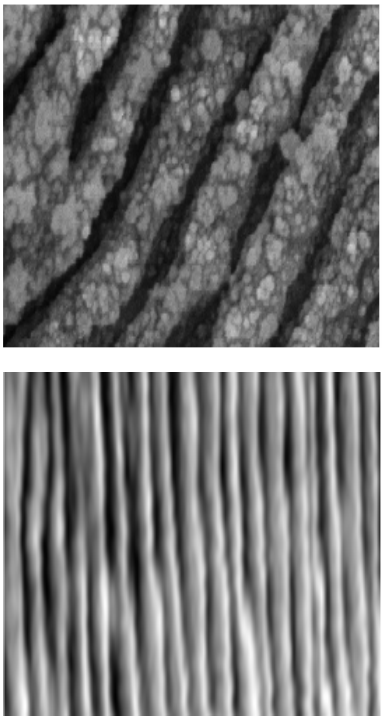

Fig. (2) The periodic structured of the irradiated cell, by a 100fs laser pulses, 800nm wavelength, 4μm length (above) and 12μm length (below)

3. Results and Discussion

Effects of the irradiation of the spectral response for samples before and after ultrashort laser pulses irradiation are shown in Fig. (3). This figure shows the dependence of the responsivity versus wavelength and the role of the laser effects at room temperature.

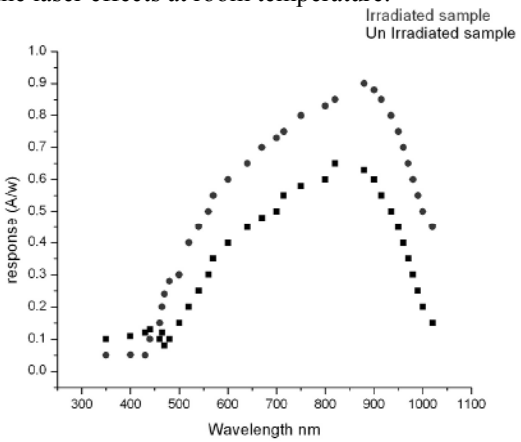

Fig. (3) The spectral response of the irradiated (upper curve) and unirradiated (lower curve) photovoltaic solar cells

The relative response increased after the irradiation processes. From this figure one can observe that the efficiency of the irradiated sample is enhanced clearly compared to unirradiated sample at the wavelengths longer than 500nm. The responsivity of the photovoltaic cell hence is increased from 0.18A/W to 0.25A/W due to irradiation effect. The

conversion efficiency of the irradiated cell is calculated using the well known equation

$$\eta = \frac{IV}{AI_o}$$

where I is the current value, V is the voltage, I_o is the solar intensity and A is the solar cell area.

The results show that the measured efficiency for the bare Silicon solar cell was 9% before irradiation and tend to be 14% after that; however the area under the response curves as shown in Fig. (4) indicating that the total response of the irradiated samples at different wavelengths.

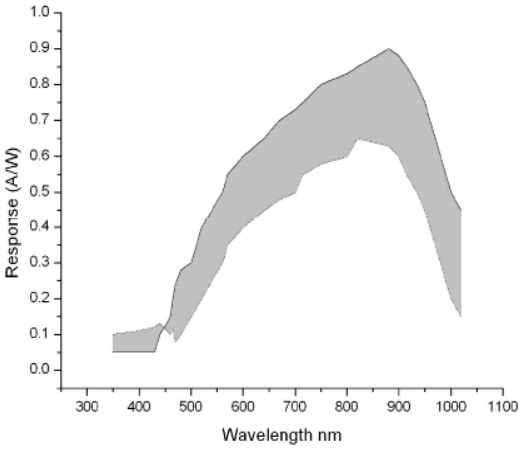

Fig. (4) The comparison of the spectral response curve of irradiated and unirradiated solar cells

The ratio of the total quantum yield obtained before and after irradiation yield a 1.43 times increases in the total efficiency of the solar cell along the whole spectral wavelength range of the working solar cell. On the other hand, the gain response curves as a function of the bias voltage for irradiated sample at different wavelength are shown in Fig. (5).

4. Conclusions

In summary, we have demonstrated how we can perform sub-microstructure of photovoltaic cell by means of irradiating the sample by femtosecond laser pulses. The responsivity and the conversion efficiency of the photovoltaic cell are enhanced by this technique.

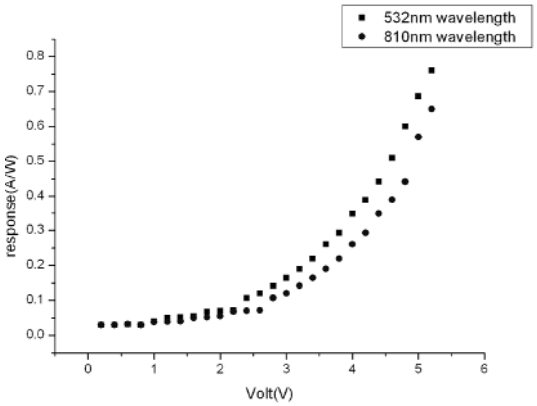

Fig. (5) The gain response of irradiated and unirradiated samples at two different wavelengths

Acknowledgment

Authors acknowledge M. Bellini and A. Zavatta for their help during the irradiation the samples. K.A.N. acknowledges ICTP for the financial support in the framework of the TRIL program.

References

[1] T. Kubarsepp., P. Karha., and E. Ikonen, *Appl. Opt.*, 39 (2000) 1.
[2] J.E. Carey et al., *Opt. Lett.,* 30 (2005) 1773.
[3] C.H. Crouch et al., *Appl. Phys. Lett.*, 84 (2004) 1850.
[4] Z. Jingtao et al., *SPIE*, 10, 1117/12, 57 (2005) 1965. Lasers in Material Processing and Manufacturing II. Edited by Deng, ShuShen; Matsunawa, Akira; Yao, Y. Lawrence; Zhong, Minlin. Proc. of the SPIE, Vol. 5629 (2005) 276-283.
[5] R.A. Myers et al., *Appl. Opt.*, 45 (2006) 35.

OSA Optical Society of America
FORTHCOMING CONFERENCES

International Optoelectronics Exhbition (InterOpto)
Chiba, Japan
Sep 09 - 11 2009

9th International Conference on Correlation Optics (Correlation Optics 09)
Chernivtsi, Ukraine
Sep 20 - 24 2009
Submission Deadline: 3/1/2009
Registration Deadline: 8/20/2009

International Symposium on Optical Memory 2009 (ISOM)
Nagasaki, Japan
Oct 04 - 08 2009
Submission Deadline: 5/29/2009

All-Russian Conference on Fiber Optics
Perm, Russian Federation
Oct 08 - 09 2009
Submission Deadline: 6/15/2009
Registration Deadline: 9/10/2009

Advances in Optical Materials (AIOM)
San Jose, California United States
Oct 11 - 15 2009
Submission Deadline: 5/27/2009

Computational Optical Sensing and Imaging (COSI)
San Jose, California United States
Oct 11 - 14 2009
Submission Deadline: 5/27/2009
Post Submission Deadline: 9/21/2009

Signal Recovery and Synthesis (SRS)
San Jose, California United States
Oct 12 - 13 2009
Submission Deadline: 5/27/2009
Post Submission Deadline: 9/21/2009

Adaptive Optics: Methods and Analysis (AO)
San Jose, California United States
Oct 12 - 14 2009
Submission Deadline: 5/27/2009
Post Submission Deadline: 9/21/2009

15th Microoptics Conference (MOC '09)
Tokyo, Japan
Oct 25 - 28 2009

The Second International Workshop on Theoretical and Computational Nano-Photonics (TaCoNa-Photonics)
Bad Honnef, Germany
Oct 28 - 30 2009
Submission Deadline: 8/1/2009
Housing Deadline: 10/1/2009
Registration Deadline: 10/1/2009

International Conference on Optics and Photonics (ICOP)
Chandigarh, India
Oct 30 - 01 2009
Submission Deadline: 4/15/2009
Registration Deadline: 9/30/2009

Annual Directed Energy Symposium
San Antonio, Texas United States
Nov 02 - 06 2009
Submission Deadline: 6/15/2009
Registration Deadline: 10/29/2009

Introduction to Illumination Design Using LightTools® (ORA)
Pasadena, California United States
Nov 02 - 04 2009

Asia Communications and Photonics Conference and Exhibition (ACP)
Shanghai, China
Nov 02 - 06 2009
Submission Deadline: 6/9/2009

Advanced Topics in LightTools®: COM Macro Programming and Optimization (ORA)
Pasadena, California United States
Nov 05 - 06 2009

Optimization of Composition, Structure and Characteristics of Metal in Arc Deposition

Vladimir Jakovlev
Stanislaw Shanchurov

Physical Engineering Faculty ,
Ural State Technical University,
Ekaterinburg 620002,
Uralmash, Russian Federation

In this work, the chemical composition of carbide was changed at shock loading. The formation of austenite from ferrite or pearlite and the change of carbide composition runs as a result of diffusion processes, therefore it was supposed, that as a result of micro- and macro-plastic metal deformation, which is conducted by heat-evolution, the iron diffusivity in local amounts of the alloy should increase considerably and therefore it should be dissolved in carbides. The increase of iron contents took place in carbides of M_7C_3 and $M_{23}C_6$ as a result of tempering or contact-shock circular loadings at the expenses of diffusion processes. It was explained that strengthening phase of developed alloy 2M3 was carbides MC, M_7C_3 and $M_{23}C_6$.

Keywords: Arc deposition, Composition, Structure, Metal Characteristics
Received: 27 January 2009, **Revised**: 11 February 2009, **Accepted**: 18 February

1. Introduction

The scientific-technical revolution started by the direct application of physics in engineering. The amazing developments in the past three decades was, to a large extent, due to the achievements of materials science and technology, i.e., due to the fact that knowledge about the microphysics of matter allowed the design of processes which made new type of materials properties available to applications. Cars are getting lighter and lighter by the introduction of new ceramics and light metal processing techniques, materials in integrated circuits are now designed almost with “atomic” precision, single crystals can be produced in the shape of huge turbine blades, erbium doped optical fibres work on long distances, even low cost diamond layers are within reach. Besides the traditional fields of engineering, new materials and processes enter the medical practice (implants, artificial organs, diagnose and operation techniques).

The solidification of melts belongs to the most frequently used methods of materials processing (casting of metals, welding, soldering, etc.). In the last decades, rapid progress has been achieved in the improvement of several conventional technologies and new methods have been developed due to the better understanding of the mechanism of solidification. In metallurgy, the use of continuous casting is growing rapidly. The general trend is to reduce the forming processes in a solid state (forging, rolling, machining).

It is known that economically alloyed manganese steels with a structure of martensite, 20-25% of retained austenite and with carbide strengthening are perspective for roller conveyers deposition. Deposited metal with hardness of 38-43HRC is satisfactory treated by blade instrument [1]. That is why when developing the optimum composition of surfacing alloy there were limitations on the amount of retrained austenite, hardness and contents of molybdenum, nickel and niobium in deposited metal.

2. Experiment

The influence of alloying element change on deformability of deposited metal at high temperatures, on wear resistance, on hardness and on the amount of retained austenite was held by method of experiment multiple-factor planning. 29 compositions of deposited metal were studied. Surfacing alloy was got by electric arc deposition of cordless wire on plates from steel 20 of size 400x250x40mm. Deposition was made with using of flux AN-20 under conditions: I=360-400A, U=30-32V, welding speed is 24m/h, number of layers are 8.

Regression equations allow evaluating the influence of alloying elements on investigated metal characteristics after deposition. Numerical experiments were held for the following compositions of surfacing alloys: carbon – 0.38%, chromium – 5.6%, manganese – 4.0%, molybdenum – 0.72%, nickel – 0.84%, niobium – 0.82%. In the process of experiments

concentration of two elements were changing, and the contents of the rest was constant.

3. Results and Discussion

The hardness of deposited metal increases with the raise of amount of carbon and manganese in it, and the given hardness interval moves to the range of higher concentrations of these elements and has a "C" – shape appearance (Fig. 1). With a carbon contents of 0.42% the hardness 43HRS is corresponded to two concentrations of manganese – 4.1 and 5.1%. Apparently, this can be explained, that in deposited metal almost all carbon is joint in carbides. That is why when increasing its amount the hardness raises not much and it does not influence on the amount of retained austenite in deposited metal.

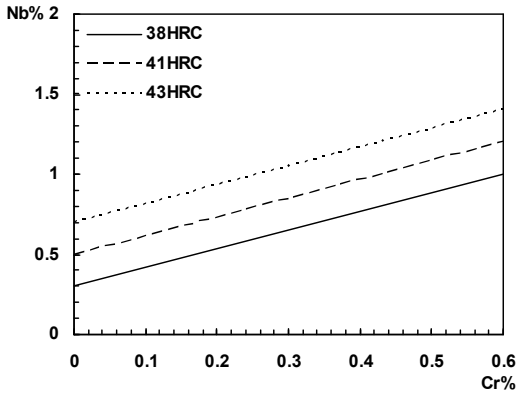

Fig. (1) Influence of alloying Nb-Cr elements on the hardness of deposited metal at 20°C

With the raise of manganese concentration the amount of retained austenite in the structure increases, and the hardness decreases. In a similar way the level lines of hardness are changed with the raise of manganese and chromium (Fig. 2). The original influence of these elements is also explained by retained austenite formation.

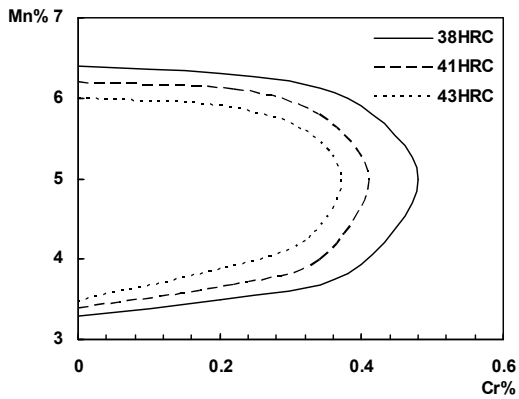

Fig. (2) Influence of alloying Mn-Cr elements on the hardness of deposited metal at 20°C

In the developed surfacing alloy molybdenum, apparently, does not form independent carbides, and together with nickel alloys a hard solution and almost does not influence on hardness. Niobium increases hardness (Fig. 3), however, its growth with the increases of carbon contents is not great. This certifies that when surfacing part of niobium is fixed in hard solution and does not form carbides. Therefore in the process of tempering dispersion strengthening of deposited metal should be expected.

Relative wear resistance of deposited metal increases with the raise of carbon, chromium, niobium and decreases with the raise of manganese and molybdenum. Obviously, in deposited alloy chromium and niobium form carbides, which increase wear resistance. In the concentration range of 1-2% the increase of niobium contents does not change wear resistance with carbon raise. Then wear resistance falls because of carbides size growth and its' intensive chipping in wear process.

Taking into account the limitations on metal hardness after deposition (38-43HRC) and on the contents of such alloying elements as niobium, molybdenum and nickel in surfacing alloy, and also on the amount of retained austenite (20-25%), the problem of optimization of deposited metal composition was solved. The object was to get the highest dynamic "hot" hardness at 600°C. As a result the following optimum composition of economically alloyed surfacing alloy was obtained: carbon – 0.38%, chromium – 5.6%, manganese – 4.0%, molybdenum – 0.72%, nickel – 0.84%, niobium – 0.82%. This composition was symbolically named – 2M3.

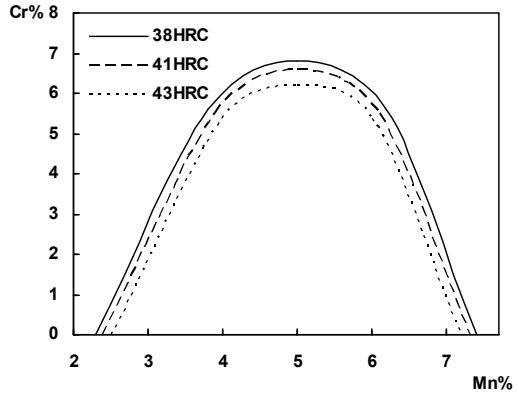

Fig. (3) Influence of alloying Cr-Mn elements on the hardness of deposited metal at 20°C

Numerical experiments showed that carbon, niobium, chromium and molybdenum increase dynamic "hot" hardness, and then resistance of metal deformation at high temperature. Apparently, this is connected with the formation of heat-resistant carbides, and also alloying of

hard solution by molybdenum, chromium and niobium. The raise of manganese concentration at 0.2-0.3% of carbon decreases the resistance of deformation. However, with increase of carbon contents its negative influence declines, and at 0.55% C stops to affect.

It ensures the following characteristics of the deposited metal: $345HD_{600}$, 42HRC, relative wear resistance at 20°C is ε=4.2, amount of retained austenite – 23.6%. The change of carbon concentration by ±0.02%, of chromium and manganese – by ±0.5%, nickel and niobium – by ±0.3% causes the change of hardness by not more than 2%, and of the other characteristics by 8-10%.

Earlier it was supposed that for roller conveyers' deposition it should be perspective to use economically alloyed manganese steel of the following composition: carbon – 0.25-0.35%, manganese – 5.0-6.0%, molybdenum – 0.8-1.3%, vanadium – up to 1.0%, niobium – 0.5-1.0%, which was symbolically named – 1M3. Surfacing alloy of 3Cr2V8 type [2-4] is widely adopted for roller deposition, and cordless wire PP-25Cr5VMoSi [5,6] is used for details strengthening, operating under similar conditions. Therefore the research of mechanical and wear-resistant characteristics of 1M3 and 2M3 surfacing alloys will be held together with deposited metal of 25Cr5VMoSi and 3Cr2V8 types.

It is impossible to predict uniquely the chemical and phase composition of second phase rejections in surfacing complex-alloyed alloys. Therefore there was held a determination of phase and chemical compositions of the rejections. Large, medium and fine-dispersed rejections of the second phase are seen in fractures of the pattern.

Tempering of deposited metal of 2M3 and 1M3 types at temperature of 500°C during 8 hours causes the hardness increase of developed alloys. The hardness change of deposited metal is a result of the decay of retained austenite and dispersion strengthening. The analysis of carbide residue, rejected from surfacing 2M3 alloy before and after heat treatment showed the presence of carbides of MC, M_7C_3 and $M_{23}C_6$ types. After heat treatment a percentage contents of carbides in the alloy increases approximately by 20-25% and reaches 13-15 mass percents. Therefore it can be supposed, that hardness increase of investigated surfacing alloys is a result of carbide dispersion rejections. The results of X-ray spectrometry microanalysis from replica showed that chemical composition of carbides of M_7C_3 and $M_{23}C_6$ types is changed after heat treatment of surfacing 2M3 alloy. X-ray investigation of iron has appeared, which did not take place in the initial patterns, carved from deposited metal. Iron erosion in carbides during the process of alloy heat treatment is connected with the initial stage of their coagulation, which was increased in comparison with other alloying elements by diffusion rate of iron in steel and by density of martensite crystal boundaries [7], i.e. basically it is determined by diffusion processes.

The temperature rises in steels with strongly different in plastic deformation structural phase components [8]. Heat, basically, is released at plastic deformation of soft component. Cravz-Tarnovskiy discovered that local heat build-up and change of metal structure takes place at single impact deformation of patterns of pearlitic steel. Investigations, which were held by Davidenkov [10] and Pridansev [11], showed that at impact compression of pearlite-ferrite, sorbite and other steels a heat build-up of local amounts of metal up to approximately 1250°C takes place. As a result martensite interlayer of 0.02-0.9mm thick are formed. The formation of austenite from ferrite or pearlite [12] and the change of carbide composition runs as a result of diffusion processes, therefore it was supposed, that as a result of micro- and macro-plastic metal deformation, which is conducted by heat-evolution, the iron diffusivity in local amounts of the alloy should increase considerably and therefore it should be dissolved in carbides.

4. Conclusion

In concluded remarks, the chemical composition of carbide is changed at shock loading. Strengthening phase of developed alloy 2M3 is carbides MC, M_7C_3 and $M_{23}C_6$. The increase of iron contents takes place in carbides of M_7C_3 and $M_{23}C_6$ as a result of tempering or contact-shock circular loadings at the expenses of diffusion processes.

Acknowledgement

Authors would like to thank Prof. I. Sorokov and Prof. Ali K. Mohammad for their valuable comments and advice. Also, they would like to thank the Editorial Bard of

References

[1] G.S. Gun, V.E. Sokolov and N.N. Ogarkov, "Roll treatment", *Metallurgy*, 34 (1983) 15-21.

[2] I.A Utin and G.I. Shandarenko, *Automat. Weld.*, 5 (1969) 344-350.

[3] M.A. Tylkin, "Strength and wear resistance of metallurgical equipment parts", *Metallurgy*, 16 (1965) 1-7.

[4] M.A. Tylkin and V.I. Sivak, *Weld. Prod.*, 10 (1959) 37-39.

[5] M.A. Tylkin, "Reference book for heat-treator for repair service" *Metallurgy*, 32 (1981) 22-29.

[6] I.I. Frumin, "Contemporary types of deposited metal and their classification", Theoretical and technological bases of deposition, Deposited Metal, Kiev (1977) 3-9.
[7] M.I. Goldstein and V.M. Farber, "Dispersion steel strengthening", *Metallurgy*, 30 (1979) 6-11.
[8] B.P. Zaitsev and K.E. Bondarev, "Mosaic of temperatures and instant resistance of 2nd genre at impact deformation of two-phase metal", Phys. of Metals and Metal Sci., 3 (1956) 139-145.
[9] V.P. Cravz-Tarnovskiy, "A specific line in steel", *Rus. Metallur. Commun.*, 3 (1928) 162.
[10] N.N. Davidenkov and I.N. Mirolyubov, "A special type of steel impact deformation", *Mess. Metal Indust.*, 5 (1930) 57-59.
[11] M.V. Pridansev and V.N. Kopernikova, "Steel structure after fast plastic deformation", *Metal Sci. Heat Treat. of Metals*, 5 (1979) 57-59.
[12] I.I. Novikov, "Theory of heat treatment of metals", *Metallurgy*, 34 (1983) 33-38.

The Use of Laser, Nanotechnology to Rapidly Detect Viruses

Waiting a day or more to get lab results back from the doctor's office soon could become a thing of a past. Using nanotechnology, a team of University of Georgia researchers has developed a diagnostic test that can detect viruses as diverse as influenza, HIV and RSV in 60 seconds or less. In addition to saving time, the technique could save lives by rapidly detecting a naturally occurring disease outbreak or bioterrorism attack.

"It saves days to weeks," said lead author Ralph Tripp, Georgia Research Alliance Eminent Scholar in Vaccine Development at the UGA College of Veterinary Medicine. "You could actually apply it to a person walking off a plane and know if they're infected." The technique, called surface enhanced Raman spectroscopy (SERS), works by measuring the change in frequency of a near-infrared laser as it scatters off viral DNA or RNA. This phenomenon is well known, but failed because the signal produced is inherently weak. The research group experimented several different metals and methods and found that placing rows of silver nanorods 10,000 times finer than the width of a human hair on the glass slides that hold the sample could enhance the signal. They found that the signal is best amplified when the nanorods are arranged at an 86-degree angle.

The technique is so powerful that it has the potential to detect a single virus particle and can also discern virus subtypes and those with mutations such as gene insertions and deletions. This specificity makes it valuable as a diagnostic tool, but also as a means for epidemiologists to track where viruses originate from and how they change as they move through populations. The researchers have shown that the technique works with viruses isolated from infected cells grown in a lab, and the next step is to study its use in biological samples such as blood, feces or nasal swabs. Preliminary results are so promising that it could be possible to create an online encyclopedia of Raman shift values. With that information, a technician could readily reference a Raman shift for a particular virus to identify an unknown virus.

Presently, viruses are first diagnosed with methods that detect the antibodies a person produces in response to an infection. These tests are prone to false positives because a person can still have antibodies in their system from a related infection decades ago. The tests are also prone to false negatives because some people don't produce high levels of antibodies. Because of these limitations, antibody based tests often must be confirmed with a test known as polymerase chain reaction (PCR), which detects the virus itself by copying it many times. The test can take anywhere from several days to two weeks, a too long period, especially in light of emerging threats such as H5N1 avian influenza.

COPYRIGHT RELEASE
Iraqi Journal of Applied Physics (IJAP)

We, the undersigned, the author/authors of the article titled
……
……
……
……
……
……
that is presented to the Iraqi Journal of Applied Physics (IJAP) for publication, declare that we have neither taken part or full text from any published work by others, nor presented or published it elsewhere in any other journal. We also declare transferring copyrights and conduct of this article to the Iraqi Journal of Applied Physics (IJAP) after accepting it for publication.

The authors will keep the following rights:
1. **Possession of the article such as patent rights.**
2. **Free of charge use of the article or part of it in any future work by the authors such as books and lecture notes without referring to the IJAP.**
3. **Republishing the article for any personal purposes of the authors after taking journal permission.**

To be signed by all authors:

Signature:……..date: ……..

Printed name: ……

Signature:……..date: ……..

Printed name: ……..

Signature:……..date: ……..

Printed name: ……..

Correspondence address:
……
……
……
Address:……
……
……
Telephone:……..email: ……..

Note: Please complete and sign this form and mail it to the below address with your manuscript

The Iraqi Journal of Applied Physics
P. O. Box 55259, Baghdad 12001, IRAQ
Website: www.ijap.org
Email: editor@ijap.org
Phone: +964 7901274190

 ISSN 1813-2065

IRAQI JOURNAL OF APPLIED PHYSICS

CONTENTS